Article:

Pedatella, NM, Liu, H-L, Marsh, DR orcid.org/0000-0001-6699-494X et al. (5 more authors) (2018) Analysis and Hindcast Experiments of the 2009 Sudden Stratospheric Warming in WACCMX+DART. Journal of Geophysical Research: Space Physics, 123 (4). pp. 3131-3153. ISSN 2169-9402

https://doi.org/10.1002/2017JA025107

Analysis and Hindcast Experiments of the 2009 Sudden Stratospheric Warming in WACCMX+DART

N. M. Pedatella [1,2], H.-L Liu [1], D. R. Marsh [1,3], K. Raeder [4], J. L. Anderson [4], J. L. Chau [5], L. P. Goncharenko [6], and T. A. Siddiqui [1]

[1]High Altitude Observatory, National Center for Atmospheric Research, Boulder, Colorado, USA.
[2]COSMIC Program Office, University Corporation for Atmospheric Research, Boulder, Colorado, USA.
[3]Atmosphere Chemistry Observations and Modeling, National Center for Atmospheric Research, Boulder, Colorado, USA.
[4]Computational Information Systems Laboratory, National Center for Atmospheric Research, Boulder, Colorado, USA.
[5]Leibniz Institute of Atmospheric Physics, Rostock University, Kühlungsborn, Germany
[6]Haystack Observatory, Massachusetts Institute of Technology, Westford, Massachusetts, USA.

Key Points:

- Initial results of a whole atmosphere-ionosphere data assimilation model, WACCMX+DART
- Middle and upper atmosphere variability is well reproduced in WACCMX+DART analysis fields
- SSW and associated middle and upper atmosphere variability can be forecast ~10 days in advance

Corresponding author: N. M. Pedatella, `nickp@ucar.edu`

Abstract

The ability to perform data assimilation in the Whole Atmosphere Community Climate Model eXtended version (WACCMX) is implemented using the Data Assimilation Research Testbed (DART) ensemble adjustment Kalman filter. Results are presented demonstrating that WACCMX+DART analysis fields reproduce the middle and upper atmosphere variability during the 2009 major sudden stratospheric warming (SSW) event. Compared to specified dynamics WACCMX, which constrains the meteorology by nudging towards an external reanalysis, the large-scale dynamical variability of the stratosphere, mesosphere, and lower thermosphere are improved in WACCMX+DART. This leads to WACCMX+DART better representing the downward transport of chemical species from the mesosphere into the stratosphere following the SSW. WACCMX+DART also reproduces most aspects of the observed variability in ionosphere total electron content (TEC) and equatorial vertical plasma drift during the SSW. Hindcast experiments initialized on January 5, 10, 15, 20, and 25 are used to assess the middle and upper atmosphere predictability in WACCMX+DART. A SSW, along with the associated middle and upper atmosphere variability, is initially predicted in the hindcast initialized on January 15, which is ~10 days prior to the warming. However, it is not until the hindcast initialized on January 20 that a major SSW is forecast to occur. The hindcast experiments reveal that dominant features of the TEC can be forecast ~10-20 days in advance. This demonstrates that whole atmosphere models that properly account for variability in lower atmosphere forcing can potentially extend the ionosphere-thermosphere forecast range.

1 Introduction

In contrast to the lower atmosphere, where model initialization and model physics are critical components to extending the useful forecast range [*Magnusson and Källén*, 2013], forecasting the ionosphere-thermosphere beyond ~24-48 hours is largely dependent on adequately forecasting the drivers of upper atmosphere variability. The dominant drivers are forcing from solar/geomagnetic activity and waves propagating upwards from the lower atmosphere. Forecasting the ionosphere-thermosphere beyond a few days therefore requires forecasting the solar/geomagnetic activity and the lower atmosphere variability. This is not to say that initial conditions are unimportant for ionosphere-thermosphere forecasting; rather, beyond a few hours for the ionosphere and several days for the thermosphere they have minimal impact on forecast skill compared to externally forced variability

[*Jee et al.*, 2007; *Chartier et al.*, 2013]. There is therefore a need for improved forecasting of the solar/geomagnetic and lower atmosphere drivers of ionosphere-thermosphere variability. Although there have long been efforts focused on predictions of solar and geomagnetic activity [e.g., *Feynman and Gu*, 1986; *Joselyn*, 1995], there are comparatively few investigations into improved ionosphere-thermosphere forecasts through enhancing predictions of the lower atmosphere forcing. This is despite the fact that lower atmosphere variability contributes to a significant portion of the day-to-day variability in the ionosphere, especially during solar quiet time periods [*Rishbeth and Mendillo*, 2001; *Liu*, 2016]. Furthermore, aspects of lower atmosphere variability, such as sudden stratospheric warming (SSW) events, can be predicted beyond the 5-7 day troposphere forecast skill [e.g., *Tripathi et al.*, 2015], and they are known to introduce variability in the ionosphere of up to 100% [*Goncharenko et al.*, 2010; *Chau et al.*, 2011].

Data assimilation models focused on the ionosphere-thermosphere [e.g., *Scherliess et al.*, 2006; *Lee et al.*, 2012; *Matsuo et al.*, 2013] have typically only incorporated the climatological effects of lower atmosphere variability into the forecast model. This potentially limits the forecast skill, especially during time periods that are dominated by lower atmosphere driven variability. However, recent developments in whole atmosphere modeling [*Akmaev*, 2011] offer the opportunity to enhance the predictability of the ionosphere-thermosphere. This is due to the ability of whole atmosphere models to forecast the lower atmosphere variability along with its impact on the ionosphere-thermosphere. The potential benefits of this approach were demonstrated by *Wang et al.* [2011] and *Wang et al.* [2014], who were able to predict the ionosphere variability during the 2009 SSW using the National Oceanic and Atmospheric Administration (NOAA) Whole Atmosphere Model (WAM) as forcing for an ionosphere-plasmasphere model. It was demonstrated that the ionosphere variability could be predicted in forecasts initialized 10 days prior to the peak of the SSW event. To our knowledge, this is the only previous demonstration that incorporating lower atmosphere driven variability can extend the range of ionosphere-thermosphere forecasts.

The present study reports on the initial results of a whole atmosphere-ionosphere data assimilation system that can potentially enhance predictability of the upper atmosphere through forecasting the effects of variability driven by the lower atmosphere. Specifically, the Data Assimilation Research Testbed (DART) [*Anderson et al.*, 2008] ensemble adjustment Kalman filter (EAKF) is used to constrain the lower and middle atmosphere variability in the Whole Atmosphere Community Climate Model eXtended version (WACCMX) [*Liu et al.*, 2017]. Though potentially useful as a forecast model, it should also be noted that the analysis fields generated by the data assimilation can be used for scientific investigations of ionosphere-thermosphere variability during specific time periods. We focus our attention on the 2009 SSW time period, and demonstrate that the WACCMX+DART analysis fields reproduce the middle atmosphere chemical and dynamical variability, as well as variability in ionosphere vertical drifts and electron densities. A series of ensemble hindcasts are also performed in order to investigate the predictability of the middle and upper atmosphere during the 2009 SSW event.

The remainder of the paper is organized as follows. Section 2 describes the WACCMX+DART forecast model and data assimilation methodology. Results for the WACCMX+DART analysis and hindcast experiments are described in Sections 3.1 and 3.2, respectively. The results are discussed in Section 4. Conclusions of the study are given in Section 5.

2 WACCMX+DART Model and Data Assimilation Description

The forecast model used for the experiments is WACCMX version 2.0, which is described in detail by *Liu et al.* [2017]. Briefly, WACCMX extends from the surface to 4.1×10^{-10} hPa (~500-700 km), and incorporates the chemical, dynamical, and physical processes necessary to model the troposphere, stratosphere, mesosphere, thermosphere and ionosphere. Up to the lower thermosphere, the model is based on the Whole Atmosphere Community Climate Model (WACCM) version 4 [*Marsh et al.*, 2013], which is the 'high-top' extension of the Community Atmosphere Model version 4 (CAM4) [*Neale et al.*, 2013]. Ionospheric processes, including ionosphere transport for O^+, self-consistent electrodynamics, and energetics in WACCMX version 2.0 are primarily based on the Thermosphere-Ionosphere-Electrodynamics General Circulation Model (TIE-GCM) [*Roble et al.*, 1988; *Richmond et al.*, 1992; *Qian et al.*, 2014]. The reader is referred to *Liu et al.* [2017], and references therein, for a more detailed description of WACCMX.

Specific details regarding the WACCMX configuration used in the present study are as follows. The WACCMX horizontal resolution is 1.9° in latitude and 2.5° in longitude. The model has 126 vertical levels, with a varying vertical resolution of roughly 1.1-3.5 km in the lower atmosphere, and 0.25 scale height above 0.96 hPa (~50 km). When generating the analysis fields, WACCMX is forced with realistic solar and geomagnetic conditions. Geomagnetic activity is included by imposing the Heelis empirical convection pattern [*Heelis et al.*, 1982], which is driven by the three hour geomagnetic K_p index, at high-latitudes. The effects of solar irradiance are incorporated using the models of *Lean et al.* [2005] and *Solomon and Qian* [2005]. Since it is known to be enhanced during SSW events, we have added forcing of the migrating semidiurnal lunar tide ($M2$) based on *Pedatella et al.* [2012]. Greenhouse gases and ozone depleting substances are specified based on historical values. WACCMX+DART was initialized on October 1, 2008 by applying small perturbations to the temperature and winds in a free-running, single-member, transient WACCMX simulation. In evaluating the analysis fields, we use hourly WACCMX+DART output despite using a six hour data assimilation cycle. This is done to provide sufficient temporal resolution for evaluating certain aspects of the results. The results presented in Section 3.1 are therefore a combination of analyses and short-term (1-5 h) forecasts.

For the hindcast experiments that are presented in Section 3.2, 27-day lagged solar and geomagnetic forcing parameters are used in WACCMX. This amounts to a persistence forecast of solar activity based on the average solar rotation period. Analyzed sea surface temperatures (SSTs) [*Hurrell et al.*, 2008] are used for both the analysis and hindcast experiments. Because we have used analyzed SSTs, our hindcasts could not actually be made in real time. However, forecasts of SST (and even persistence forecasts) for lead times of a few weeks are very skillful [*Sooraj et al.*, 2012]. We would therefore only anticipate a small impact from using forecasted instead of analyzed SSTs for WACCMX forecasts.

The data assimilation is incorporated in WACCMX using the DART EAKF [*Anderson*, 2001; *Anderson et al.*, 2008]. The DART EAKF was previously used to perform data assimilation in WACCM, and we employ a nearly identical setup as previously used in WACCM+DART [*Pedatella et al.*, 2014a, 2016]. We similarly use an ensemble size of 40, and assimilate observations of aircraft and radiosonde temperatures and winds, satellite drift winds, Constellation Observing System for Meteorology, Ionosphere, and Climate (COSMIC) refractivity, and temperatures from Aura Microwave Limb Sounder (MLS) and Thermosphere Ionosphere Mesosphere Energetics Dynamics (TIMED) satellite Sounding of the Atmosphere using Broadband Emission Radiometry (SABER). The MLS and SABER temperatures are assimilated up to 1×10^{-3} hPa (~95 km) and 5×10^{-4} hPa (~100 km), respectively. The WACCMX ionosphere is thus not directly constrained by observations; rather it is responding to forcing from the constrained lower atmosphere, as well as solar forcing. Observations are localized in the vertical direction using a Gaspari-Cohn function [*Gaspari and Cohn*, 1999] with a half width of 0.15 in $ln(p_o/p)$ coordinates, where p is pressure and p_o is surface pressure, and 0.2 radians horizontally. Following *Pedatella et al.* [2014a], spatially and temporally varying adaptive inflation [*Anderson*, 2009] is used with the inflation damping set to 0.7, and a lower bound of 0.6 for the inflation standard deviation.

We note that there are two changes in WACCMX+DART that have a negative impact on the data assimilation. In order to damp small-scale (considered here to be wavenumbers greater than 6) waves, we apply both second- and fourth-order divergence damping [*Lauritzen et al.*, 2012]. The second-order divergence damping is applied in addition to the fourth-order divergence damping, which is the default for WACCMX, in order to remove longer wavelength waves that are not effectively damped by the fourth-order divergence damping. The additional second-order divergence damping attenuates waves with wavenumbers of ~1-30. The fourth-order damping is also applied since it more effectively removes resolved-scale waves with wavenumbers greater than ~30. The small-scale waves that are introduced by the data assimilation pose two problems for WACCMX. First, the electrodynamics solver can fail if the small-scale waves are sufficiently large in the thermosphere. Second, and perhaps more important, the small-scale waves considerably increase the mixing in the lower thermosphere. The increased mixing leads to a reduction in the ratio of atomic oxygen to molecular nitrogen (O/N_2) in the thermosphere, which will reduce the electron density [*Yamazaki and Richmond*, 2013; *Siskind et al.*, 2014]. The effects of the small-scale waves and resultant increase in mixing are significant, and the O/N_2 ratio and electron density can be reduced by up to ~50% in WACCMX+DART experiments that do not effectively damp the small-scale waves. Although the increased damping negatively impacts the model performance, it was necessary in order to prevent large decreases in O/N_2 ratio and electron density. There is an additional minor degradation in the tropospheric data assimilation in WACCMX+DART compared to WACCM+DART due to the 5-minute time step used in WACCMX (a 30-minute time step is used in WACCM). The shorter time step leads to a ~30% bias in troposphere humidity. The humidity bias is related to the CAM4 physics parameterizations. We confirmed that the time step is the source of this bias through a comparison of WACCM+DART experiments with 5- and 30-minute time steps. The bias between WACCM+DART run with 5- and 30-minute time steps is similar to that between WACCMX+DART and WACCM+DART, and we thus concluded that the humidity bias is directly due to the change in model time step.

To illustrate the impact of the above changes on the troposphere data assimilation, Figure 1 shows profiles of the six-hour analysis and forecast root mean square error (RMSE) and bias relative to radiosonde temperature observations in the Northern and Southern Hemisphere extratropics (±20-80°). The results are averaged for December 2008, and are shown for both WACCM+DART (black) and WACCMX+DART (red). Note that the results in Figure 1 are based on the subset of observations that were assimilated in both experiments. From these plots it is clear that there is a ~5-10% increase in forecast RMSE in WACCMX+DART compared to WACCM+DART. The difference is larger in the Northern Hemisphere compared to the Southern Hemisphere, though this may partly be due to seasonal differences. Although there is a slight degradation in the WACCMX+DART troposphere, the synoptic scales that are likely to be the dominant source of the middle and upper atmosphere variability (at least in a relatively coarse resolution model such as WACCMX) remain well captured in WACCMX+DART. The degraded troposphere is therefore considered to have minimal influence on the middle and upper atmosphere, which are the primary focus of our study.

3 Results

3.1 2009 SSW Analysis Fields

The evolution of the high-latitude Northern Hemisphere zonal mean temperatures averaged between 70-90°N and zonal wind at 60°N in WACCMX+DART are presented in Figures 2 and 3. The results in Figures 2 and 3, and throughout the following, are for the WACCMX+DART ensemble means. Also included in Figures 2 and 3 are results from a specified dynamics simulation of WACCMX (SD-WACCMX). The SD-WACCMX meteorology is constrained up to 50 km by nudging towards the National Aeronautics and Space Administration (NASA) Modern-Era Retrospective Analysis for Research and Applications (MERRA) [*Rienecker et al.*, 2011]. SD-WACCMX represents an alternative, computationally less expensive, approach for reproducing specific time periods in WACCMX. It thus represents a useful benchmark for comparison with WACCMX+DART. The Aura MLS observed variability is also shown in Figure 2c (note that the model is not sampled directly at the observation locations, so some sampling error may be present in Figure 2). The evolution of the stratosphere and lower mesosphere polar temperatures (Figure 2) is similar between SD-WACCMX and WACCMX+DART. This is to be expected since both are constrained at these altitudes, and it is also consistent with prior comparisons between SD-WACCM and WACCM+DART [*Pedatella et al.*, 2014a]. Differences between the SD-WACCMX and WACCMX+DART become more apparent at higher altitudes. Notable differences include a stronger mesosphere cooling in WACCMX+DART around the peak of the SSW (days 20-25), as well as a warmer mesopause following the SSW in WACCMX+DART. Additionally, the elevated stratopause that forms in early February gradually decreases in altitude in WACCMX+DART. In contrast, the elevated stratospause in SD-WACCMX exhibits an initial rapid decrease in altitude between days 30 and 40. The gradual decrease in stratopause altitude in WACCMX+DART is more consistent with the Aura MLS observations (Figure 2c). As noted in *Pedatella et al.* [2014a] the mesospheric differences are directly related to the assimilation of Aura MLS and TIMED/SABER temperatures in WACCMX+DART, and the inclusion of these observations leads to improved representation of the stratosphere-mesosphere variability throughout the 2009 SSW time period. Comparison of the zonal mean zonal winds at 60°N (Figure 3) shows largely similar behavior as the temperatures, with differences between WACCMX+DART and SD-WACCMX again emerging above 1 hPa (∼50 km). In this case, the most apparent differences are weaker westward winds in the stratosphere during the SSW, as well as a stronger mesosphere wind reversal between days ∼20-34 in WACCMX+DART.

The elevated stratopause following the 2009 SSW led to enhanced descent of mesospheric air into the stratosphere. This is clearly captured in satellite observations that show descent of nitrogen oxides (NO_x = NO + NO_2) and carbon monoxide (CO) into the stratosphere following the SSW [*Manney et al.*, 2009; *Randall et al.*, 2009]. The enhanced descent is generally poorly captured by constrained chemistry climate models [e.g., *Funke et al.*, 2017], which can partly be attributed to inaccurate representation of the dynamics in the upper stratosphere-mesosphere due to lack of direct constraint at these altitudes [*Siskind et al.*, 2015]. The ability to accurately reproduce enhanced NO_x and CO descent is therefore a useful indirect method for assessing the large-scale dynamics in the mesosphere. Figure 4 shows the 70-90°N zonal mean NO in SD-WACCMX and WACCMX+DART, and clearly illustrates that there is considerably greater NO descent in late February to early March in WACCMX+DART compared to SD-WACCMX. The improved representation of NO descent in WACCMX+DART is related to better representation of the elevated stratopause in this simulation [e.g., *Meraner et al.*, 2016]. Odin Sub-Millimeter Radiometer (SMR) observations in Figure 2 of *Funke et al.* [2017] show that NO of 0.1 ppmv descends to almost 0.1 hPa (~65 km). By comparison, at 0.1 hPa the WACCMX+DART NO is 0.02-0.05 ppmv. The downward transport of NO may therefore still be underestimated in WACCMX+DART, though we note that this is not a direct comparison since the simulation results were not sampled at the satellite observation locations. We should also note that the NO deficit may not be entirely related to underestimating the downward transport. Rather, it could be related to errors in chemical reaction rates or incorrect specification of energetic particle precipitation. While both of these versions of WACCMX include NO_x production from auroral electrons, the pattern of precipitation is highly idealized and the precipitating electrons have a fixed characteristic energy of 2 keV. Additionally, we have not included the production of NO_x by medium energy (up to 1 MeV) electrons that penetrate into the mesosphere. Improving the characterization of these processes is the subject of ongoing research.

The temporal variability of the migrating diurnal tide ($DW1$) and combined migrating semidiurnal solar and lunar tide ($SW2 + M2$) in temperature are shown in Figures 5 and 6, respectively. To look at variations on shorter time scales, we do not attempt to separate the semidiurnal solar and lunar tide contributions due to their similar periodicities (12 h and 12.42 h). We note that the $M2$ lunar tide is not included in the SD-WACCMX physics, though it may be indirectly forced in the model through being present in reanalysis fields that are used for nudging [*Kohyama and Wallace*, 2014]. Though included in the WACCMX+DART physics, the $M2$ lunar tide may also be present in WACCMX+DART analysis fields through the assimilation of observations (though it would not be present in the hindcast experiments without being included in the WACCMX+DART physics). The results are shown at 0.01 hPa (~80 km) for $DW1$ and $1{\times}10^{-4}$ hPa (~110 km) for $SW2 + M2$ to be comparable with previous simulation results shown in *Pedatella et al.* [2014a] and *Pedatella et al.* [2014b]. Similar temporal variability of $DW1$ and $SW2 + M2$ occurs in both SD-WACCMX and WACCMX+DART, and the variability is similar to other whole atmosphere models [*Pedatella et al.*, 2014b]. In particular, both SD-WACCMX and WACCMX+DART show a clear decrease in $DW1$ near day 30, and an increased semidiurnal tide amplitude between days 30 and 40. Although the temporal variability is similar, the tides in both SD-WACCMX and WACCMX+DART are weaker compared to results in other whole atmosphere models. This is especially true for WACCMX+DART, which has tidal amplitudes that are ~30% less than those in SD-WACCMX. We believe this to be the result of the additional damping that is included in WACCMX+DART, and will be discussed in more detail in Section 4.

We now turn our attention to the ionosphere variability during the 2009 SSW. Figures 7 and 8 show the total electron content (TEC) at 75°W geographic longitude at 1000 and 1800 local time (LT), respectively. Note that we focus our attention on this longitude sector due to the dense network of ground-based Global Navigation Satellite System (GNSS) receivers in North and South America. The GNSS TEC observations are included in Figures 7 and 8 for comparison with the simulation results. The GNSS TEC observations are based on the MIT Automated Processing of GPS (MAPGPS) software [*Rideout and Coster*, 2006]. Although the TEC exhibits variability throughout January-February 2009, the most notable TEC changes attributed to the SSW are the morning increase and afternoon decrease in TEC that occur between January 22-30 [e.g., *Goncharenko et al.*, 2010]. At 1000 LT (Figure 7), both SD-WACCMX and WACCMX+DART capture the enhancement around January 22-30, as well as the subsequent decrease and increase in TEC that occurs in the following 10-20 days. However, the initial enhancement occurs ~2-3 days earlier in the simulations compared with the observations. The results at 1800 LT (Figure 8) are generally similar, with both SD-WACCMX and WACCMX+DART exhibiting a decrease around January 22-30, but with the decrease occurring prior to what is seen in the observations. The timing discrepancy is most apparent in SD-WACCMX, and the TEC minimum occurs roughly four days prior to the observed minimum. Though it still occurs 1-2 days early, the timing of the minimum TEC in WACCMX+DART is more consistent with the observations. WACCMX+DART also better reproduces the TEC enhancement, and increased latitudinal separation of the equatorial anomalies, around days 32-35. We may therefore conclude, at least qualitatively for this event, that the WACCMX+DART ionosphere is in better agreement with observations compared to SD-WACCMX. This is also true quantitatively, and the RMSE for the low-latitude (0°N-30°S) TEC at 1000 (1800) LT is 2.47 (2.79) total electron content unit (TECU) for WACCMX+DART and 3.76 (4.68) TECU for SD-WACCMX . This demonstrates that the improved specification of the MLT that results from assimilating observations to higher altitudes also leads to an improvement in the ionosphere.

In addition to TEC, it is well known that equatorial vertical drifts are disturbed during SSWs [*Chau et al.*, 2011]. Vertical drift perturbations therefore provide another opportunity to evaluate the ionosphere variability in SD-WACCMX and WACCMX+DART. Figures 9 and 10 show the equatorial vertical drift perturbations at 75°W and 77°E geographic longitude. The perturbations are calculated from the January-February mean value at each local time. The model simulations are compared with observations from the Peruvian Jicamarca Radio Observatory (JRO, 11.95°S, 76.87°W geographic) Incoherent Scatter Radar (ISR) [*Chau et al.*, 2010], and the difference between Indian magnetometer observations at Tirunelveli (8.7°N, 77.8°E geographic) and Alibaug (18.6°N, 72.9°E geographic) [*Siddiqui et al.*, 2017]. Note that the difference between the two magnetometer stations, one on the magnetic equator and one 5-10° off the equator, is used as a proxy for variations in the vertical plasma drift velocity [*Anderson et al.*, 2002]. The agreement between SD-WACCMX and WACCMX+DART and the observations at 77°E is particularly good, with WACCMX+DART capturing much of the variability that is seen in the magnetometer observations. However, there are larger discrepancies between the simulations and observations at 75°W. Most notably, the vertical drift perturbations are $\sim$10 ms^{-1} weaker than the observed values. Additionally, the JRO ISR observations reveal an increase in the vertical drift that begins in the morning around January 25 and moves towards later local times over the next 10 days. This feature is weak in SD-WACCMX, and largely absent in WACCMX+DART, indicating that certain aspects of the ionosphere remain poorly characterized in SD-WACCMX and WACCMX+DART. There are clear differences in the vertical drift perturbations in SD-WACCMX and WACCMX+DART; however, neither appears to be in significantly better agreement with the observations. The RMSE between SD-WACCMX and WACCMX+DART and the JRO ISR observations are 10.86 ms^{-1} and 10.95 ms^{-1}, respectively. In the Indian longitude sector the RMSE is 5.04 ms^{-1} in SD-WACCMX and 5.18 ms^{-1} in WACCMX+DART (assuming that ΔH = 4.3268$\times\Delta$W$_i$ [*Anderson et al.*, 2002]). SD-WACCMX and WACCMX+DART are therefore considered as essentially identical in terms of their agreement with vertical drift observations.

3.2 2009 SSW Hindcast Experiments

As demonstrated in the previous section, the WACCMX+DART analysis fields generally reproduce the middle and upper atmosphere variability during the 2009 SSW. Given that SSWs can often be predicted 1-2 weeks in advance [*Tripathi et al.*, 2015], SSWs may afford the opportunity to extend the useful range of ionosphere forecasts, at least for solar quiescent time periods. To examine the ionosphere predictability associated with the 2009 SSW, we have performed a series of hindcast experiments for the 2009 SSW time period. The experiments consisted of 30-day hindcasts that were initialized from the analysis fields at 0000 UT on January 5, 10, 15, 20, and 25. Each hindcast included 40-ensemble members. As noted in Section 2 the hindcasts were forced with analyzed SSTs, and 27-day lagged solar and geomagnetic activity.

Figures 11 and 12 show the hindcasts for the ensemble mean zonal mean temperature averaged between 70-90°N and zonal mean zonal wind at 60°N. These can be directly compared with Figures 2 and 3. In terms of predicting the SSW, the general characteristics in temperature and zonal wind are similar. The first two hindcasts, initialized on January 5 and 10, do not predict the occurrence of a SSW. However, the hindcast initialized on January 15 shows a distinct warming of the stratosphere around January 25. The warming is accompanied by a reversal of the stratosphere-mesosphere zonal mean zonal winds, and also a mesosphere cooling. WACCMX+DART can therefore predict that the middle atmosphere will be disturbed due to a SSW ~10 days in advance. However, although this hindcast qualitatively predicts a SSW, the strength of the SSW is not correctly forecast in the ensemble mean, and the stratosphere wind reversal does not reach the 10 hPa (~30 km) level that is necessary to be considered a major SSW. The length of the disturbed stratospheric winds, as well as the occurrence of an elevated stratopause, are also not seen in the hindcast initialized on January 15. These features are, however, captured by the hindcasts initialized on January 20 and 25.

To better illustrate how the hindcasts capture the SSW induced stratosphere and mesosphere variability, Figure 13 shows the hindcasts for zonal mean zonal winds at 60°N and 10 hPa (~30 km) and zonal mean temperature at $1{\times}10^{-4}$ hPa (~110 km) averaged between 70-90°N. Note that in Figure 13, we show results for the ensemble mean as well as the standard deviation in order to illustrate differences in the ensemble spread in the stratosphere and mesosphere. The ensemble maxima and minima are also included for the stratospheric winds. In the stratosphere, the hindcasts closely follow the analysis (black dashed line) for 5-7 days before beginning to diverge. It is also clear in Figure 13a that all of the ensemble members, as well as the ensemble mean, in the hindcast initialized on January 15 only predict a minor SSW around January 25 (i.e., the winds at 60°N and 10 hPa do not reverse). The ensemble mean hindcast initialized on January 20 forecasts a major SSW, though the westward wind maximum is forecasted to occur 2-3 days later than in the analysis. Additionally, the ensemble mean forecasts maximum westward winds that are $\sim$15 ms^{-1} too weak; however, two of the ensemble members forecast maximum westward winds of -30 ms^{-1}. The extent, and recovery, of the SSW in the stratosphere are well captured in the hindcast initialized on January 25. It is interesting to note that some of the ensemble members in the hindcasts initialized on January 5 and January 15 forecast the occurrence of a major SSW towards the end of the 30-day forecast period. It is unclear whether this is indicative that a major SSW will occur in the subsequent months, or if it is only reflective of the fact that SSWs will be generated in WACCMX by the inherent atmospheric variability. The fact that these occur towards the end of the forecast period suggests the later, but additional research is required to understand if these forecasted SSWs are providing useful information.

Compared to the stratospheric winds, the behavior of the mesosphere temperatures in Figure 13 are markedly different, with the hindcasts often departing from the analysis within the first few days. This is consistent with worse predictability of the mesosphere [*Liu et al.*, 2009], though we caution that one should not make definitive conclusions on the mesosphere predictability based on the small number of hindcasts included in the present study. Figure 13 also illustrates the significant differences in the ensemble spread in the stratosphere and mesosphere. In particular, the ensemble spread in the stratosphere is initially small, and gradually increases throughout nearly the entire 30-day hindcast. In contrast, the ensemble spread in the mesosphere is comparatively larger initially and increases by a relatively small amount during the 30-day hindcast. This suggests that there is much larger uncertainty for even short-term (i.e., 1-2 days) forecasts in the mesosphere. Interestingly, the spread in the hindcast initialized on January 25 grows the least, and has the smallest spread at the end of the 30-day hindcast. The evolution of the stratosphere and mesosphere following a major SSW can therefore be forecasted with relatively small uncertainty, even for forecasts in the range of 20-30 days. Additional cases are, however, required to confirm if this is a general feature, or unique to this particular event.

The ionosphere variability during SSWs is largely driven by changes in the semidiurnal solar and lunar tides [e.g., *Pedatella and Liu*, 2013]. Any forecast of the ionosphere variability during a SSW event will therefore necessitate correctly forecasting the semidiurnal tidal variability. Hindcasts of $SW2 + M2$ are shown in Figure 14. From the analysis fields in Figure 6, the dominant features of the $SW2 + M2$ variability are a Southern

Hemisphere enhancement around day 20, Northern Hemisphere enhancement around day 30, and enhancements in both hemispheres on day 40. Aspects of the temporal variability, such as the enhancements near days 30 and 40, are seen in the hindcast initialized on January 15. However, the enhancements primarily occur in the Southern Hemisphere, and there is no enhancement near day 20. The tidal variability is correctly forecasted in the hindcasts initialized on both January 20 and January 25. Interestingly, the hindcasts initialized on January 20 and 25 forecast the tidal variability reasonably well for at least 20 days. This suggests that the forecast skill for certain aspects of mesosphere variability may be in the range of 20 days, though we again caution that one should not make firm conclusions from the limited number of hindcasts included in the present study.

We conclude our discussion of the hindcast results by demonstrating the extent that ionosphere TEC variability can be forecast in WACCMX+DART. Figures 15 and 16 show the hindcast results at 1000 and 1800 LT, respectively. One aspect of the hindcasts in the ionosphere that should be mentioned is that there tends to be an overall increase in TEC during the first several days of the hindcast. This can potentially complicate interpretation of the results. The TEC increase is related to the fact that the small-scale waves introduced by the data assimilation are absent in the hindcasts. As previously mentioned, the dissipation of small-scale waves in the lower thermosphere increases lower thermosphere mixing, leading to a reduction in the ionosphere electron density. The absence of these waves will therefore lead to an overall increase in TEC. Interpretation of the forecasted TEC variability also depends on the 27-day lagged solar/geomagnetic activity, and we note that K_p is ~4 in the hindcasts around days 20 and 30. The TEC in the hindcasts initialized on January 5 and 10 show some aspects of variability that are broadly similar to the SSW induced variability in the WACCMX+DART analysis TEC, such as the TEC decrease between days 20-30. This is despite the fact that these two hindcasts do not forecast a SSW. The variability in these two hindcasts may be due to geomagnetic activity; however, this variability could also be due to $SW2 + M2$ (Figure 14) which tends to be anticorrelated with the TEC. The hindcast initialized on January 15 appears to capture much of the ionosphere variability associated with the SSW. For example, at 1800 LT, this hindcast forecasts the TEC enhancements around days 20 and 34, and a decrease in TEC around days 26 and 40. These features are in good agreement with both the WACCMX+DART analysis TEC and observed TEC (Figure 8), indicating there is at least some degree of skill in 10-20 day ionospheric forecasts. We note that the TEC decreases around days 26 and 40 are stronger in the hindcast initialized on January 15 compared to the hindcasts initialized on January 5 and 10, demonstrating that the SSW forecasted in the hindcast initialized on January 15 leads to an improved TEC forecast. This is supported by additional experiments (not shown) initialized on January 15 and 20 with constant solar and geomagnetic activity. These experiments qualitatively forecast the effects of the SSW on the ionosphere ~10-20 days in advance, indicating that the lower atmosphere alone can provide long-range forecast skill for the ionosphere. The TEC at 1800 LT in the hindcast initialized on January 15 also tends to be anticorrelated with the hindcast $SW2 + M2$. The ability to forecast TEC may therefore be largely dependent upon the ability to forecast the middle atmosphere tidal variability. The hindcasts initialized on January 20 and 25 are also able to qualitatively forecast the TEC variability for the subsequent ~10-20 days. However, there are some clear deficiencies in the TEC hindcasts. For example, at 1800 LT, the hindcast initialized on January 25 forecasts an earlier and more rapid increase in TEC from the minimum that occurs around January 25. We attribute this discrepancy to the fact that this hindcast was initialized at a time when the TEC was decreasing, but the TEC decrease is offset by the aforementioned TEC increase that occurs due to less lower thermosphere mixing in the hindcast experiments.

To more clearly illustrate the ability of the hindcasts to forecast low-latitude TEC variability, Figure 17 shows the TEC at 75°W geographic longitude averaged over the equatorial anomaly region (30°S-0°N geographic). The features of TEC variability in the hindcasts discussed in the context of Figures 15 and 16 are again evident, though we highlight a few features that are more apparent when focusing on the low-latitude average TEC. First, the rapid increase, and overall bias, in the WACCMX+DART hindcast TEC is clearly evident. Any forecast of TEC in WACCMX+DART will predict an increase in TEC over the first several days of the forecast period, presenting an obvious problem for any attempt to forecast TEC. However, as this is a known, systematic, problem one could potentially calibrate WACCMX+DART TEC forecasts to remove the initial increase and longer term bias in TEC forecasts. It is also apparent in Figure 17 that, despite not forecasting a SSW, the hindcasts initialized on January 5 and 10 forecast much of the temporal variability in TEC at 1800 LT around the time of the SSW. We again consider this variability as partially due to the geomagnetic activity in the hindcast experiments, which has K_p of ~4 around January 20 and 30. Some of the forecasted TEC variability in the hindcasts is thus not due to the SSW, but due to geomagnetic activity. Nonetheless, it is clear that the hindcast initialized on January 15 is in better agreement with the analysis compared to the hindcasts initialized on January 5 and 10, indicating an improvement in the TEC forecast due to the minor SSW that is present in this hindcast. This highlights the fact that an accurate forecast of ionosphere variability requires both accurately forecasting the solar/geomagnetic activity as well as variability driven by the lower atmosphere.

4 Discussion

The hindcast results illustrate that the ionosphere TEC variability during the 2009 SSW can be qualitatively forecast up to 10-20 days in advance, which is well beyond what is typically considered the limit for forecasting upper atmosphere variability. This extended range of predictability is enabled by whole atmosphere-ionosphere modeling, which provides the ability to forecast the lower atmosphere variability and its impact on the ionosphere. There are, however, two important caveats to the ionosphere predictability seen in the present study. First, the solar and geomagnetic activity was largely quiet, and minimally varying, throughout the time period studied. The 27-day lagged solar and geomagnetic forcing used in the hindcast experiments therefore provides a reasonable forecast of the solar and geomagnetic forcing. The ionosphere predictability during periods with stronger, and more variable, solar and geomagnetic activity will be significantly influenced by the ability to provide an accurate forecast of the solar and geomagnetic activity. Second, the useful forecast range for SSWs is considerably greater than the average forecast range in the troposphere and stratosphere. The ionosphere predictability associated with SSWs may thus represent an upper limit. The average predictability enabled by incorporating lower atmosphere effects will likely be less than that during SSW events. It is therefore crucial to perform a significant number of hindcasts in order to determine the extent that lower atmosphere predictability translates into ionosphere predictability. Using WACCMX+DART for such experiments is advantageous since the ensemble can provide estimates of the forecast error, reducing the number of forecasts necessary to assess the predictability.

As mentioned in Section 2, the data assimilation introduces small-scale waves that lead to drastic reductions in thermosphere O/N_2 ratio and ionosphere electron density. The damping introduced in WACCMX+DART to remove these waves has a negative influence on the tidal amplitudes. The impact of small-scale waves is also problematic for thermosphere-ionosphere forecasting since their absence in forecasts leads to an increase in electron density, as well as O/N_2 ratio, over the initial 1-2 days of the forecast. These issues highlight the need to minimize the introduction of small-scale waves when applying the data assimilation increments. Introducing the increments through using an incremental analysis update (IAU) [*Bloom et al.*, 1996] procedure, or filtering the increments prior to applying them are two possible solutions for minimizing the introduction of small-scale waves. Alternatively, it may be possible to develop an improved damping scheme that has a smaller impact on the tidal amplitudes. A larger ensemble size should also reduce the noise, though this comes with additional computational expense. We are currently investigating the best approach for effectively addressing the small-scale waves in WACCMX+DART. It should be noted that we are assuming that the additional small-scale waves in WACCMX+DART are entirely unrealistic, and should be minimized. This assumption is, however, only based on their negative impact on the ionosphere-thermosphere. If they are actually representative of the true atmosphere, it would suggest that mixing due to other processes, such as parameterized gravity waves, is too large in WACCMX. We note that given the sensitivity of the thermosphere and ionosphere to wave induced mixing in the lower thermosphere [e.g., *Yamazaki and Richmond*, 2013; *Siskind et al.*, 2014], the importance of minimizing the influence of any small-scale waves in whole atmosphere-ionosphere data assimilation models is likely not limited to WACCMX+DART.

In the present study we have only assimilated observations in WACCMX+DART up to ~100 km. Ground-based observations of ionosphere TEC and COSMIC radio occultation electron density profiles have previously been assimilated in the NCAR TIE-GCM using DART [*Lee et al.*, 2012; *Chen et al.*, 2016]. It is anticipated that the assimilation of ionosphere observations in WACCMX+DART should positively impact the results. This is especially true for the analysis fields, where assimilation of ionosphere electron densities may, for example, indirectly improve the vertical plasma drift velocities through improving the ionospheric conductivity. Short-term thermosphere-ionosphere forecasts are also likely to be improved by assimilating ionosphere observations; however, they may have less influence on forecasts beyond several days. Ionosphere observations may also be able to counteract some of the negative influences of the previously mentioned small-scale waves on decreasing thermosphere O/N_2 ratio and ionosphere electron density. They therefore represent a possible approach to mitigate the negative influence of these waves on the upper atmosphere.

5 Conclusions

The present study demonstrates the ability to perform data assimilation in WACCMX using the DART EAKF. WACCMX+DART generates whole atmosphere-ionosphere analysis fields that are useful for scientific investigations, and can also be used to provide initial conditions for forecasting the middle and upper atmosphere. We demonstrate the capability of WACCMX+DART, when only assimilating observations up to ~100 km, through evaluation of analysis fields and hindcasts of the 2009 SSW. The primary conclusions are:

1. The large-scale dynamical variability of the middle atmosphere (stratosphere to lower thermosphere) is well reproduced in WACCMX+DART analysis fields. Consequently, WACCMX+DART captures the transport of chemical species from the mesosphere into the stratosphere following the 2009 SSW. The results demonstrate that the assimilation of Aura MLS and TIMED/SABER temperatures improves representation of the middle atmosphere in WACCMX+DART compared to SD-WACCMX.

2. The primary shortcoming of WACCMX+DART is weak tidal amplitudes. This is due to additional damping that was added in order to eliminate small-scale waves that, if not eliminated, drastically reduce thermosphere O/N_2 ratio and ionosphere electron density.

3. The observed ionosphere TEC and vertical drift variability during the 2009 SSW period is reproduced in WACCMX+DART, though the agreement is better for TEC compared to vertical drift. Comparisons between WACCMX+DART and SD-WACCMX reveal that the ionosphere variability in WACCMX+DART is more consistent with TEC observations. Both SD-WACCMX and WACCMX+DART are similar in terms of their agreement with vertical drift observations.

4. Hindcast experiments forecast the occurrence of a SSW, and associated middle and upper atmosphere variability, roughly 10 days prior to the SSW. However, the SSW forecasted 10 days in advance is only a minor SSW, compared to the major SSW that actually occurred.

5. During the 2009 SSW time period, the TEC variability can be qualitatively forecast 10-20 days in advance in WACCMX+DART. This may represent an extreme scenario,

and the extent to which this can be generalized is limited due to the small number of hindcasts performed in the present study.

Acknowledgments

The National Center for Atmospheric Research is sponsored by the National Science Foundation. We would like to acknowledge high-performance computing support from Cheyenne (doi:10.5065/D6RX99HX) provided by NCAR's Computational and Information Systems Laboratory. N. P. acknowledges support from National Science Foundation grant AGS-1033112. H. L. was supported in part by NASA grant NNX14AH54G, and AFOSR grant FA9550-16-1-0050. The participation of J.C . in this work is part of the project supported by the Deutsche Forschungsgemeinschaft (DFG, German Research Foundation) under SPP 1788 (DynamicEarth) - CH 1482/1-1 (DYNAMITE). LPG is supported by NASA through LWS grant NNX13AI62G and by U.S. NSF grant AGS-1343056. The Jicamarca ISR and ground-based GPS TEC data are available through the MIT Haystack Observatory Madrigal database (http://madrigal.haystack.mit.edu/ madrigal/). The magnetometer data are provided by the World Data Center for Geomagnetism (http://www.wdc.bgs.ac.uk/catalog/ master.html). Model output used in this paper are archived on the NCAR High Performance Storage System. WACCM-X and DART are open-source software with source code publicly available at the NCAR website.

References

Akmaev, R. A. (2011), Whole atmosphere modeling: Connecting terrestrial and space weather, *Rev. Geophys.*, 49(4), RG4004, doi:10.1029/2011RG000364.

Anderson, D., A. Anghel, K. Yumoto, M. Ishitsuka, and E. Kudeki (2002), Estimating daytime vertical E $\times$ B drift velocities in the equatorial F-region using ground-based magnetometer observations, *Geophys. Res. Lett., 29*(12), 1596, doi:10.1029/2001GL014562.

Anderson, J. L. (2001), An ensemble adjustment Kalman filter for data assimilation, *Mon. Wea. Rev.*, 129, 2884-2903.

Anderson, J. L. (2009), Spatially and temporally varying adaptive covariance inflation for ensemble filters, *Tellus*, 61, 72-83.

Anderson, J. L., T. Hoar, K. Raeder, H. Liu, N. Collins, R. Torn, and A. F. Arellano (2008), The data assimilation research testbed: A community data assimilation facility, *Bull. Am. Meteorol. Soc.*, 90, 1283-1296, doi:10.1175/2009BAMS2618.1.

Bloom, S. C., L. L. Takacs, A. M. da Silva, and D. Ledvina (1996), Data assimilation using incremental analysis updates, *Mon. Weather Rev.*, 124, 1256-1271.

Chartier, A. T., D. R. Jackson, and C. N. Mitchell (2013), A comparison of the effects of initializing different thermosphere-ionosphere model fields on storm time plasma density forecasts, *J. Geophys. Res.*, 118, 7329-7337, doi:10.1002/2013JA019034.

Chau, J. L., N. A. Aponte, E. Cabassa, M. P. Sulzer, L. P. Goncharenko, and S. A. González (2010), Quiet time ionospheric variability over Arecibo during sudden stratospheric warming events, *J. Geophys. Res.*, 115, A00G06, doi:10.1029/2010JA015378.

Chau, J. L., L. P. Goncharenko, B. G. Fejer, and H.-L. Liu (2011), Equatorial and low latitude ionospheric effects during sudden stratospheric warming events, *Space Sci. Rev., 168*, 385-417, doi:10.1007/s11214-011-9797-5.

Chen, C. H., C. H. Lin, T. Matsuo, W. H. Chen, I. T. Lee, J. Y. Liu, J. T. Lin, and C. T. Hsu (2016), Ionospheric data assimilation with thermosphere-ionosphere-electrodynamics general circulation model and GPS-TEC during geomagnetic storm conditions, *J. Geophys. Res.*, 121, 5708-5722, doi:10.1002/2015JA021787.

Feynman, J., and X. Yue Gu (1986), Prediction of geomagnetic activity on time scales of one to ten years, *Rev. Geophys.*, 24(3), 650-666, doi:10.1029/RG024i003p00650.

Funke, B., et al. (2017), HEPPA-II model measurement intercomparison project: EPP indirect effects during the dynamically perturbed NH winter 2008-2009, *Atmos. Chem. Phys.*, 17, 3573-3604, doi:10.5194/acp-17-3573-2017

Gaspari, G., and S. Cohn (1999), Construction of correlation functions in two and three dimensions, *Q. J. R. Meteorol. Soc., 125*(554), 723-757.

Goncharenko, L. P., A. J. Coster, J. L. Chau, and C. E. Valladares (2010), Impact of sudden stratospheric warmings on equatorial ionization anomaly, *J. Geophys. Res.*, 115, A00G07, doi:10.1029/2010JA015400.

Heelis, R. A., J. K.Lowell, and R. W.Spiro (1982), A model of the high-latitude ionosphere convection pattern, *J. Geophys. Res.*, 87, 6339-6345.

Hurrell, J. W., J. J. Hack, D. Shea, J. M. Caron, and J. Rosinski (2008), A New Sea Surface Temperature and Sea Ice Boundary Dataset for the Community Atmosphere Model, *J. Climate*, 21, 5145-5153.

Jee, G., A. G. Burns, W. Wang, S. C. Solomon, R. W. Schunk, L. Scherliess, D. C. Thompson, J. J. Sojka, and L. Zhu (2007), Duration of an ionospheric data assimilation initialization of a coupled thermosphere-ionosphere model, *Space Weather*, 5, S01004, doi:10.1029/2006SW000250.

Joselyn, J. A. (1995), Geomagnetic activity forecasting: The state of the art, *Rev. Geophys.*, 33(3), 383-401, doi:10.1029/95RG01304.

Kohyama, T., and J. M. Wallace (2014), Lunar gravitational atmospheric tide, surface to 50 km in a global, gridded data set, *Geophys. Res. Lett.*, 41, 8660-8665, doi:10.1002/2014GL060818.

Lauritzen, P. H., A. A. Mirin, J. Truesdal, K. Raeder, J. L. Anderson, J. Bacmeister, and R. B. Neale (2012), Implementation of new diffusion/ filtering operators in the CAM-FV dynamical core, *Int. J. High Perform. Comput. Appl., 26*, 63-73, doi:10.1177/1094342011410088.

Lean, J., G. Rottman, J. Harder, and G. Kopp (2005), Sorce contributions to new understanding of global change and solar variability, *Solar Physics*, 230, 27-53, doi:10.1007/s11207-005-1527-2.

Lee, I. T., T. Matsuo, A. D. Richmond, J. Y. Liu, W. Wang, C. H. Lin, J. L. Anderson, and M. Q. Chen (2012), Assimilation of FORMOSAT-3/COSMIC electron density profiles into a coupled thermosphere/ionosphere model using ensemble Kalman filtering, *J. Geophys. Res.*, 117, A10318, doi:10.1029/2012JA017700.

Liu, H.-L. (2016), Variability and predictability of the space environment as related to lower atmosphere forcing, *Space Weather*, 14, 634-658, doi:10.1002/2016SW001450.

Liu, H.-L., F. Sassi, and R. R. Garcis (2009), Error Growth in a Whole Atmosphere Climate Model, *J. Atmos. Sci.*, 66, 173-186.

Liu, H.-L. et al. (2017), Development and Validation of the Whole Atmosphere Community Climate Model with Thermosphere and Ionosphere Extension (WACCM-X), *Journal of Advances in Modeling Earth Systems*, accepted, doi:10.1002/2017MS001232.

Magnusson, L. and E. Källén (2013), Factors Influencing Skill Improvements in the ECMWF Forecasting System, *Mon. Wea. Rev.*, 114, 3142-3153.

Manney, G. L., M. J. Schwartz, K. Krüger, M. L. Santee, S. Pawson, J. N. Lee, W. H. Daffer, R. A. Fuller, and N. J. Livesey (2009), Aura Microwave Limb Sounder observations of dynamics and transport during the record-breaking 2009 Arctic stratospheric major warming, *Geophys. Res. Lett.*, 36, L12815, doi:10.1029/2009GL038586.

Marsh, D. R., M. J. Mills, D. E. Kinnison, J.-F. Lamarque, N. Calvo, and L. M. Polvani (2013), Climate Change from 1850 to 2005 Simulated in CESM1(WACCM), *J. Climate*, 26, 7372-7391, doi:10.1175/JCLI-D-12-00558.1.

Matsuo, T., I.-T. Lee, and J. L. Anderson (2013), Thermospheric mass density specification using an ensemble Kalman filter, *J. Geophys. Res.*, 118, 1339-1350 doi:10.1002/jgra.50162.

Meraner, K., H. Schmidt, E. Manzini,B. Funke, and A. Gardini (2016), Sensitivity of simulated mesospheric transport of nitrogen oxides to parameterized gravity waves, *J. Geophys. Res.*, 121, 12,045-12,061,doi:10.1002/2016JD025012

Neale, R. B., J. H. Richter, S. Park, P. H. Lauritzen, S. J. Vavrus, P. J. Rasch, and M. Zhang (2013), The mean climate of the Community Atmosphere Model (CAM4) in forced SST and fully coupled experiments, *J. Climate*, 26, 5150-5168, doi: 10.1175/JCLI-D-12-00236.1.

Pedatella, N. M., and H.-L. Liu (2013), The influence of atmospheric tide and planetary wave variability during sudden stratosphere warmings on the low latitude ionosphere, *J. Geophys. Res.*, 118, 5333-5347, doi:10.1002/jgra.50492.

Pedatella, N. M., H.-L. Liu, and A. D. Richmond (2012), Atmospheric semidiurnal lunar tide climatology simulated by the Whole Atmosphere Community Climate Model, *J. Geophys. Res.*, 117, A06327, doi:10.1029/2012JA017792.

Pedatella, N. M., K. Raeder, J. L. Anderson, and H.-L. Liu (2014), Ensemble data assimilation in the Whole Atmosphere Community Climate Model, *J. Geophys. Res.*, 119, 9793-9809, doi:10.1002/2014JD021776.

Pedatella, N. M., et al. (2014), The neutral dynamics during the 2009 sudden stratosphere warming simulated by different whole atmosphere models, *J. Geophys. Res.*, 119, 1306-1324, doi:10.1002/2013JA019421.

Pedatella, N. M., J. Oberheide, E. K. Sutton, H.-L. Liu, J. L. Anderson, and K. Raeder (2016), Short-term nonmigrating tide variability in the mesosphere, thermosphere, and ionosphere, *J. Geophys. Res.*, 121, doi:10.1002/2016JA022528.

Qian, L. Y., A. G. Burns, B. A. Emery, B. Foster, G. Lu, A. Maute, A. D. Richmond, R. G. Roble, S. C. Solomon, and W. Wang (2014), The NCAR TIE-GCM: A community model of the coupled thermosphere/ionosphere system, Modeling the Ionosphere-Thermosphere System, in *Modeling the Ionosphere and Thermosphere System*, edited by J. Huba, R. Schunk, and G. Khazanov, Geophysical Monograph Series, chap. 7, p. 73, Americal Geophysical Union, doi:10.1002/9781118704417.ch7.

Randall, C. E., V. L. Harvey, D. E. Siskind, J. France, P. F. Bernath, C. D. Boone, and K. A. Walker (2009), NOx descent in the Arctic middle atmosphere in early 2009, *Geophys. Res. Lett.*, 36, L18811, doi:10.1029/2009GL039706.

Roble, R. G., E. C. Ridley, A. D. Richmond and R. E. Dickinson (1988), A coupled thermosphere/ionosphere general circulation model, *Geophys. Res. Lett.*, 15, 1325-1328.

Richmond, A. D.., E. C. Ridley, and R. G. Roble (1992), A thermosphere/ionosphere general circulation model with coupled electrodynamics, *Geophys. Res. Lett.*, 6, 601-604.

Rideout, W., and A. Coster (2006), Automated GPS processing for global total electron content data, *GPS Solutions, 10*(3), 219-228, doi:10.1007/s10291-006-0029-5.

Rienecker et al. (2011), MERRA: NASA's Modern-Era Retrospective Analysis for Research and Applications, *J. Climate*, 24, 3624-3648, doi:10.1175/JCLI-D-11-00015.1

Rishbeth, H., and M. Mendillo (2001), Patterns of ionospheric variability, *J. Atmos. Solar Terr. Phys.*, 63, 1661-1680.

Scherliess, L., R. W. Schunk, J. J. Sojka, D. C. Thompson, and L. Zhu (2006), Utah State University Global Assimilation of Ionospheric Measurements Gauss-Markov Kalman filter model of the ionosphere: Model description and validation, *J. Geophys. Res.*, 111, A11315, doi:10.1029/2006JA011712.

Siddiqui, T. A., C. Stolle, and H. Lühr (2017), Longitude-dependent lunar tidal modulation of the equatorial electrojet during stratospheric sudden warmings, *J. Geophys. Res.*, 122, 3760-3776, doi:10.1002/2016JA023609.

Siskind, D. E., D. P. Drob, K. F. Dymond, and J. P. McCormack (2014), Simulations of the effects of vertical transport on the thermosphere and ionosphere using two coupled models, *J. Geophys. Res.*, 119, 1172-1185, doi:10.1002/2013JA019116.

Siskind, D. E., F. Sassi, C. E. Randall, V. L. Harvey, M. E. Hervig, and S. M. Bailey (2015), Is a high-altitude meteorological analysis necessary to simulate thermosphere-stratosphere coupling?, *Geophys. Res. Lett.*, 42, 8225-8230, doi:10.1002/2015GL065838.

Solomon, S. C., and L. Qian (2005), Solar extreme-ultraviolet irradiance for general circulation models, *J. Geophys. Res.*, 110, A10306, doi:10.1029/2005JA011160.

Sooraj, K.P., H. Annamalai, A. Kumar, and H. Wang (2012) A Comprehensive Assessment of CFS Seasonal Forecasts over the Tropics, *Wea. Forecasting*, 27, 3-27.

Tripathi, O. P., et al. (2015), The predictability of the extratropical stratosphere on monthly time-scales and its impact on the skill of tropospheric forecasts. *Q.J.R. Meteorol. Soc.*, 141, 987-1003.

Wang, H., T. J. Fuller-Rowell, R. A. Akmaev, M. Hu, D. T. Kleist, and M. D. Iredell (2011), First simulations with a whole atmosphere data assimilation and forecast system: The January 2009 major sudden stratospheric warming, *J. Geophys. Res.*, 116, A12321, doi:10.1029/2011JA017081.

Wang, H., R. A. Akmaev, T.-W. Fang, T. J. Fuller-Rowell, F. Wu, N. Maruyama, and M. D. Iredell (2014), First forecast of a sudden stratospheric warming with a coupled whole-atmosphere/ionosphere model IDEA, *J. Geophys. Res.*, 119, 2079-2089, doi:10.1002/2013JA019481.

Yamazaki, Y., and A.?D. Richmond (2013), A theory of ionospheric response to upward-propagating tides: Electrodynamic effects and tidal mixing effects, *J. Geophys. Res.*, 118, 5891-5905, doi:10.1002/jgra.50487.

Figure 1. Root mean square error of 6-hour ensemble mean forecasts and analyses with respect to radiosonde temperature observations in the (a) Northern Hemisphere, and (b) Southern Hemisphere. Results are averaged for December 2008.

Figure 2. Zonal mean temperature during January-February 2009 averaged between 70-90°N in (a) SD-WACCMX, (b) WACCMX+DART and (c) Aura MLS observations.

Figure 3. Zonal mean zonal wind during January-February 2009 at 60°N in (a) SD-WACCMX and (b) WACCMX+DART.

Figure 4. Zonal mean nitric oxide (NO) during November 2008-March 2009 averaged between 70-90°N in (a) SD-WACCMX and (b) WACCMX+DART.

Figure 5. Diurnal migrating solar tide in temperature (a) amplitude in SD-WACCMX, (b) phase in SD-WACCMX, (c) amplitude in WACCMX+DART, and (d) phase in WACCMX+DART. Results are shown at 0.01 hPa.

Figure 6. Semidiurnal migrating solar and lunar tides in temperature (a) amplitude in SD-WACCMX, (b) phase in SD-WACCMX, (c) amplitude in WACCMX+DART, and (d) phase in WACCMX+DART. Results are shown at 1×10^{-4} hPa.

Figure 7. TEC at 75°W geographic longitude and 1000 LT for (a) SD-WACCMX, (b) WACCMX+DART, and (c) GNSS TEC observations.

Figure 8. TEC at 75°W geographic longitude and 1800 LT for (a) SD-WACCMX, (b) WACCMX+DART, and (c) GNSS TEC observations.

Figure 9. Change in the vertical plasma drift velocity at 75°W geographic longitude and 12°S geographic latitude for (a) SD-WACCMX, and (b) WACCMX+DART. (c) Change in vertical plasma drift velocity measured by the Jicamarca incoherent scatter radar. Changes are calculated relative to the January-February 2009 mean value at each local time.

Figure 10. Change in the vertical plasma drift velocity at 77°E geographic longitude and 8°N geographic latitude for (a) SD-WACCMX, and (b) WACCMX+DART. (c) Difference in the horizontal component of the geomagnetic field between Tirunelveli and Alibaug. Changes are calculated relative to the January-February 2009 mean value at each local time.

Figure 11. Zonal mean temperature during January-February 2009 averaged between 70-90°N for hindcasts initialized on (a) January 5, (b) January 10, (c), January 15, (d) January 20, and (e) January 25.

Figure 12. Zonal mean zonal wind during January-February 2009 at 60°N for hindcasts initialized on (a) January 5, (b) January 10, (c), January 15, (d) January 20, and (e) January 25.

Figure 13. (a) Zonal mean zonal wind at 60°N and 10 hPa in the WACCMX+DART analysis (dashed black) and hindcast experiments. (b) Same as (a) except for the zonal mean temperature averaged between 70-90°N at $1{\times}10^{-4}$ hPa. Solid colored lines indicate the ensemble mean, and dark shading represents ±1 standard deviation. The light shading in (a) indicates the ensemble maxima and minima.

Figure 14. Semidiurnal migrating solar and lunar tide amplitude in temperature at $1{\times}10^{-4}$ hPa for hindcasts initialized on (a) January 5, (b) January 10, (c), January 15, (d) January 20, and (e) January 25.

Figure 15. TEC at 75°W geographic longitude and 1000 LT for hindcasts initialized on (a) January 5, (b) January 10, (c), January 15, (d) January 20, and (e) January 25.

Figure 16. TEC at 75°W geographic longitude and 1800 LT for hindcasts initialized on (a) January 5, (b) January 10, (c), January 15, (d) January 20, and (e) January 25.

Figure 17. (a) TEC at 75°W geographic longitude and 1000 LT in the WACCMX+DART analysis (dashed black) and hindcast experiments. (b) Same as (a) except for the TEC at 1800 LT. Results are averaged between 30°S and 0°N geographic latitude. Dashed colored lines indicate the ensemble mean, and shading represents ±1 standard deviation.

Figure 1.

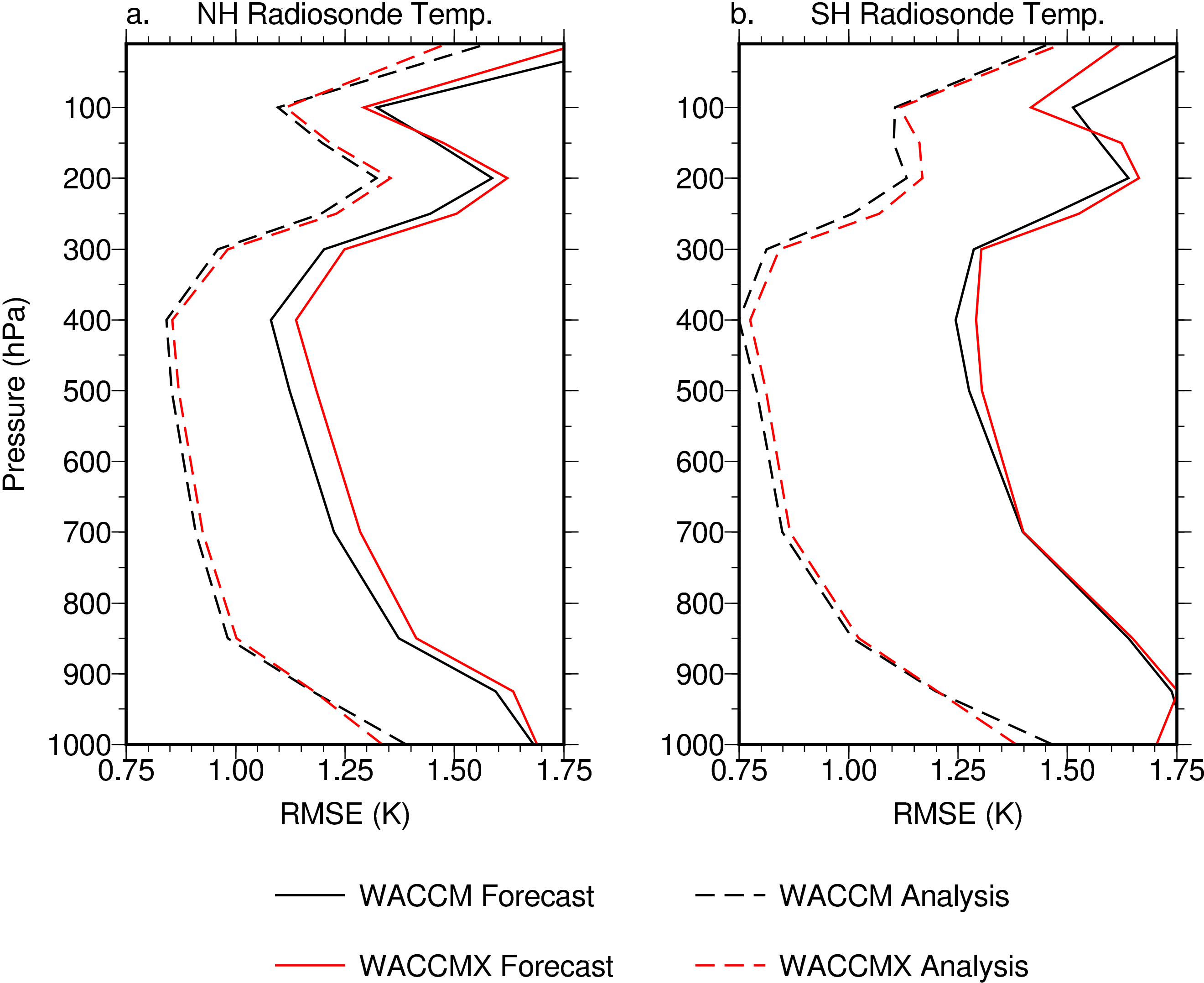
a. NH Radiosonde Temp.
b. SH Radiosonde Temp.
Pressure (hPa)
100
200
300
400
500
600
700
800
900
1000
0.75
1.00
1.25
1.50
1.75
RMSE (K)
WACCM Forecast
WACCM Analysis
WACCMX Forecast
WACCMX Analysis

Figure 2.

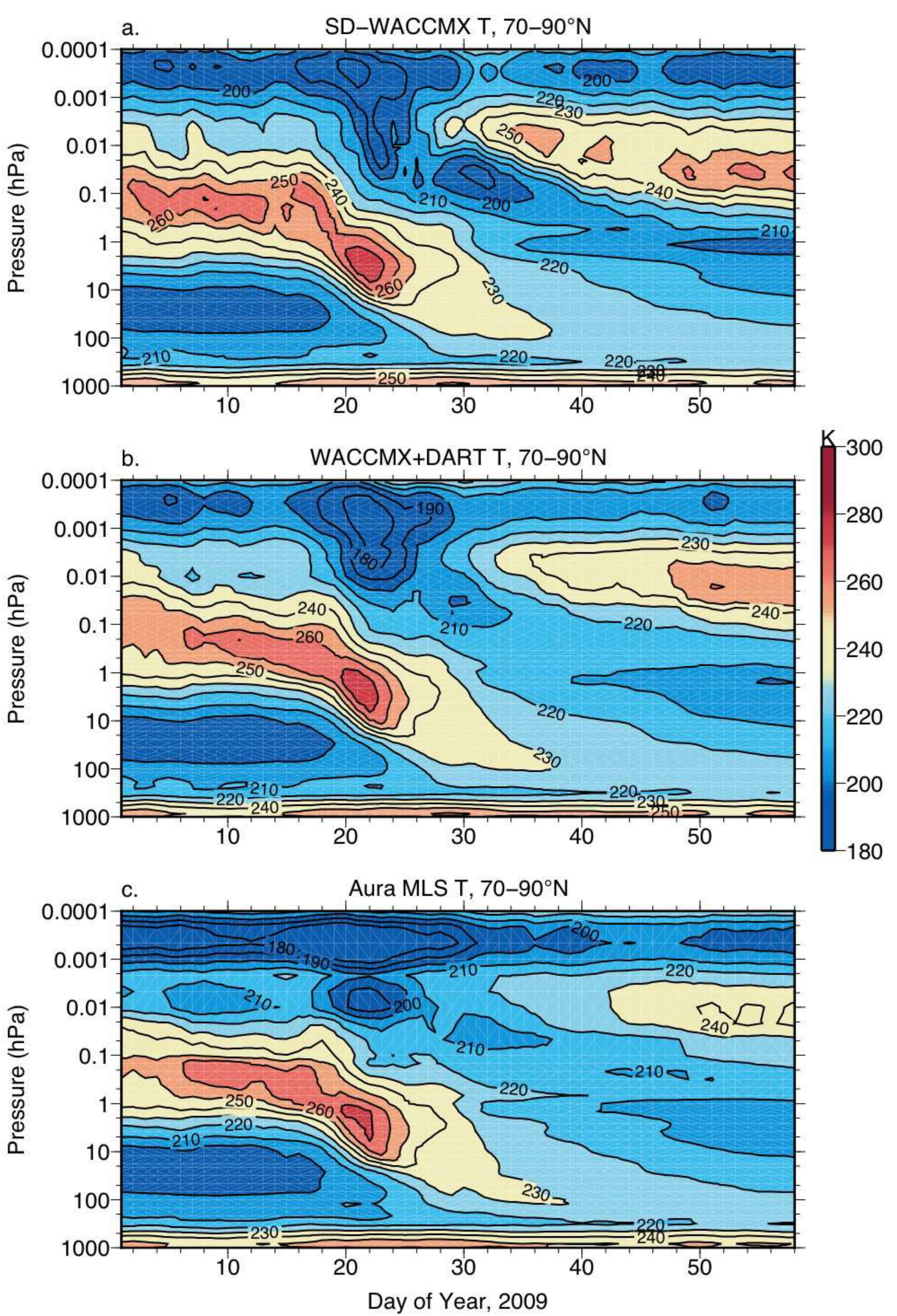

a.
SD−WACCMX T, 70−90°N
b.
WACCMX+DART T, 70−90°N
c.
Aura MLS T, 70−90°N
Pressure (hPa)
0.0001
0.001
0.01
0.1
1
10
100
1000
10
20
30
40
50
Day of Year, 2009
K
300
280
260
240
220
200
180

Figure 3.

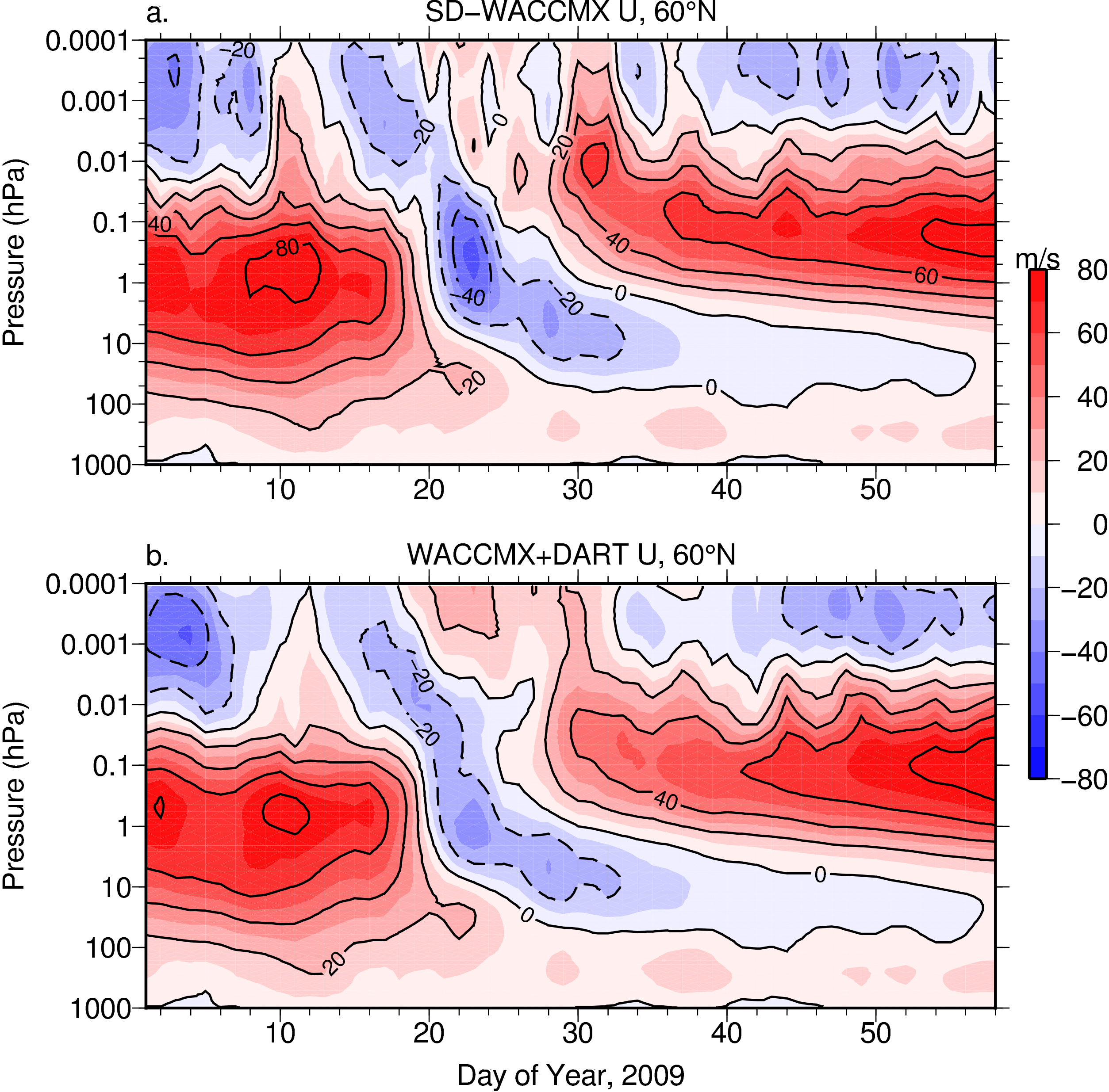

a.
SD−WACCMX U, 60°N
b.
WACCMX+DART U, 60°N
Pressure (hPa)
0.0001
0.001
0.01
0.1
1
10
100
1000
10
20
30
40
50
Day of Year, 2009
m/s
80
60
40
20
0
−20
−40
−60
−80

Figure 4.

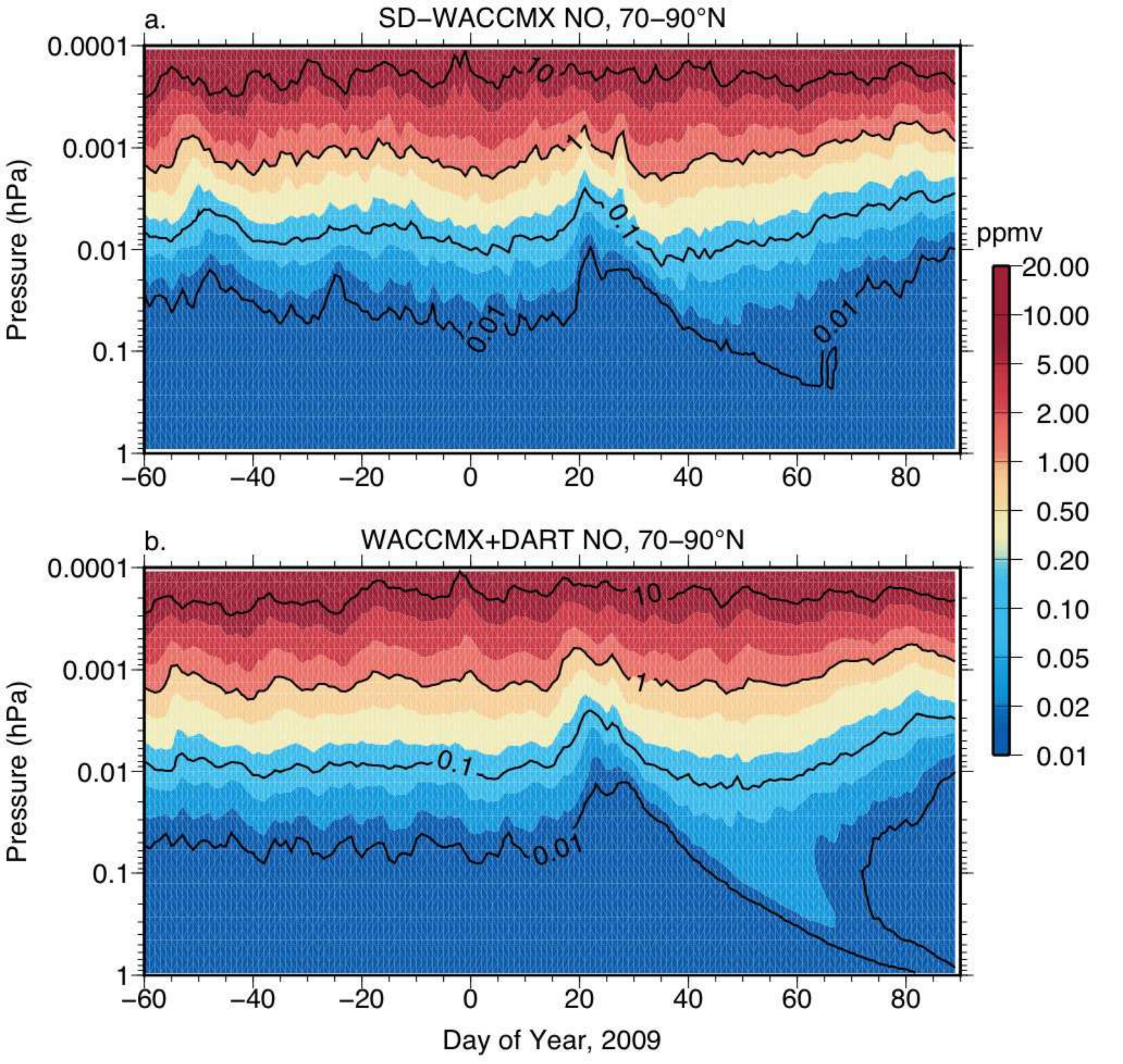
a.
SD−WACCMX NO, 70−90°N
b.
WACCMX+DART NO, 70−90°N
Pressure (hPa)
0.0001
0.001
0.01
0.1
1
10
1
0.1
0.01
−60
−40
−20
0
20
40
60
80
Day of Year, 2009
ppmv
20.00
10.00
5.00
2.00
1.00
0.50
0.20
0.10
0.05
0.02
0.01

Figure 5.

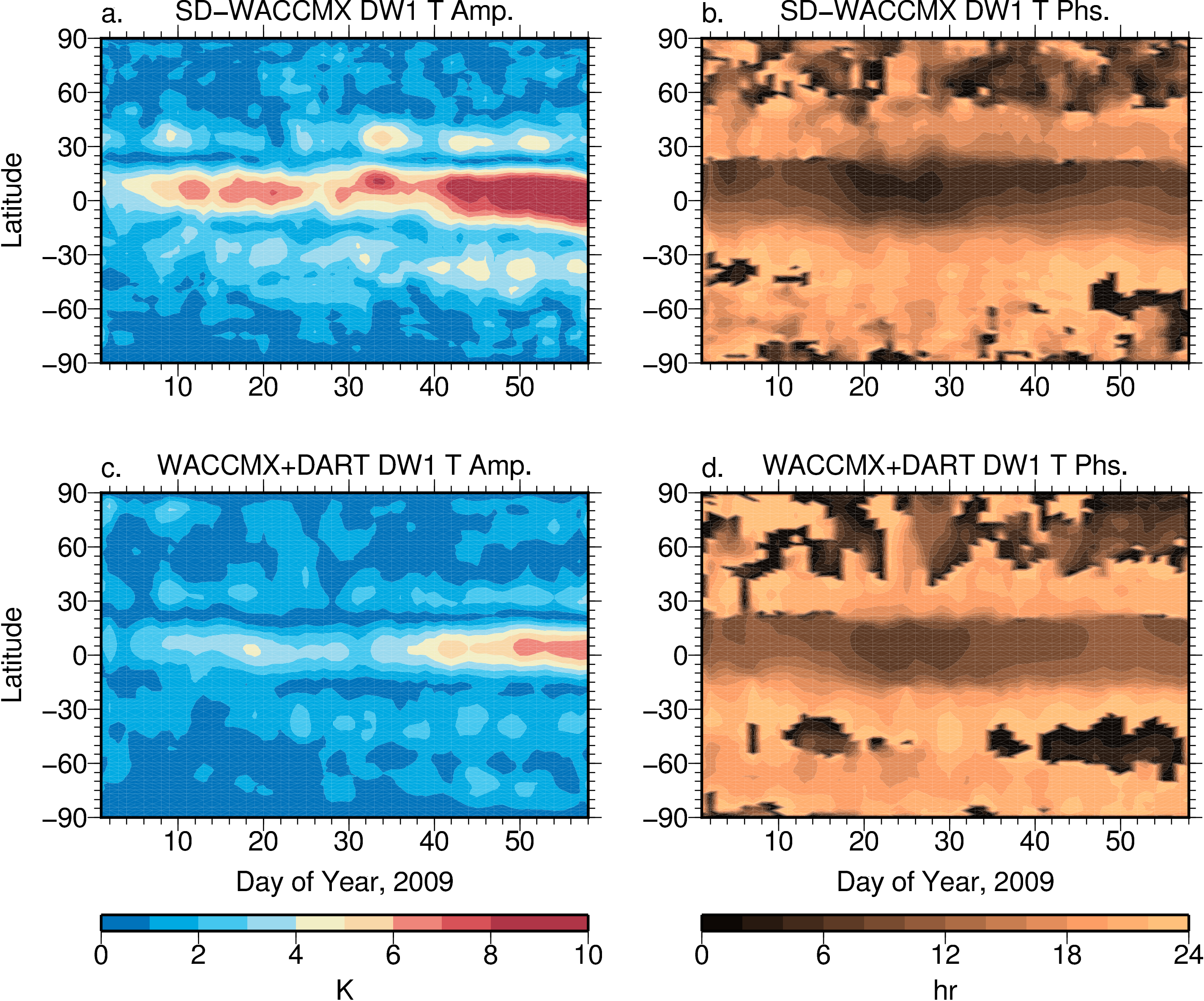
a. SD−WACCMX DW1 T Amp.
b. SD−WACCMX DW1 T Phs.
c. WACCMX+DART DW1 T Amp.
d. WACCMX+DART DW1 T Phs.
Latitude
90
60
30
0
−30
−60
−90
10
20
30
40
50
Day of Year, 2009
0
2
4
6
8
10
K
0
6
12
18
24
hr

Figure 6.

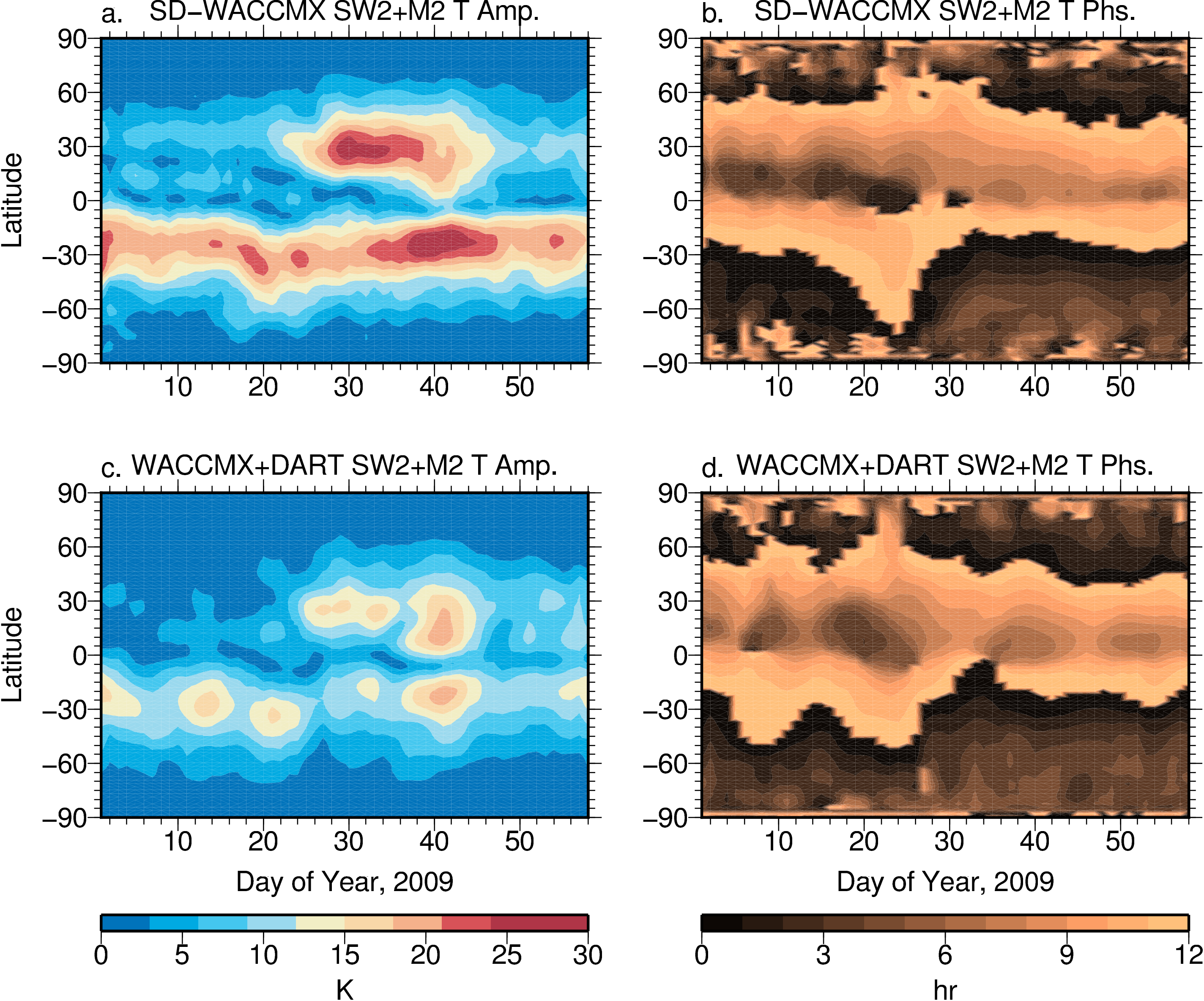

a. SD−WACCMX SW2+M2 T Amp.
b. SD−WACCMX SW2+M2 T Phs.
c. WACCMX+DART SW2+M2 T Amp.
d. WACCMX+DART SW2+M2 T Phs.
Latitude
90
60
30
0
−30
−60
−90
10
20
30
40
50
Day of Year, 2009
0
5
10
15
20
25
30
K
0
3
6
9
12
hr

Figure 7.

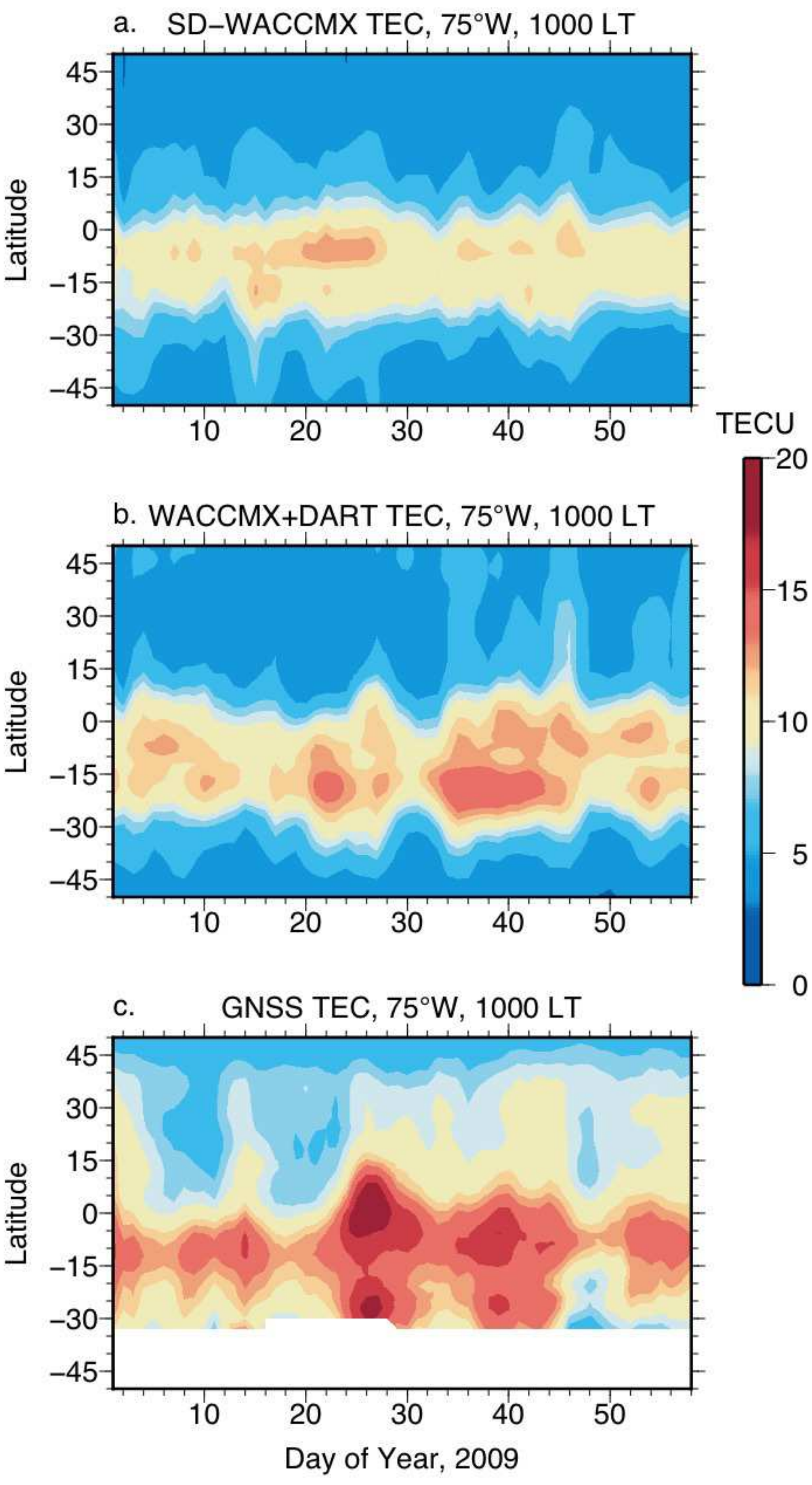

a. SD−WACCMX TEC, 75°W, 1000 LT
b. WACCMX+DART TEC, 75°W, 1000 LT
c. GNSS TEC, 75°W, 1000 LT
Latitude
45
30
15
0
−15
−30
−45
10
20
30
40
50
Day of Year, 2009
TECU
20
15
10
5
0

Figure 8.

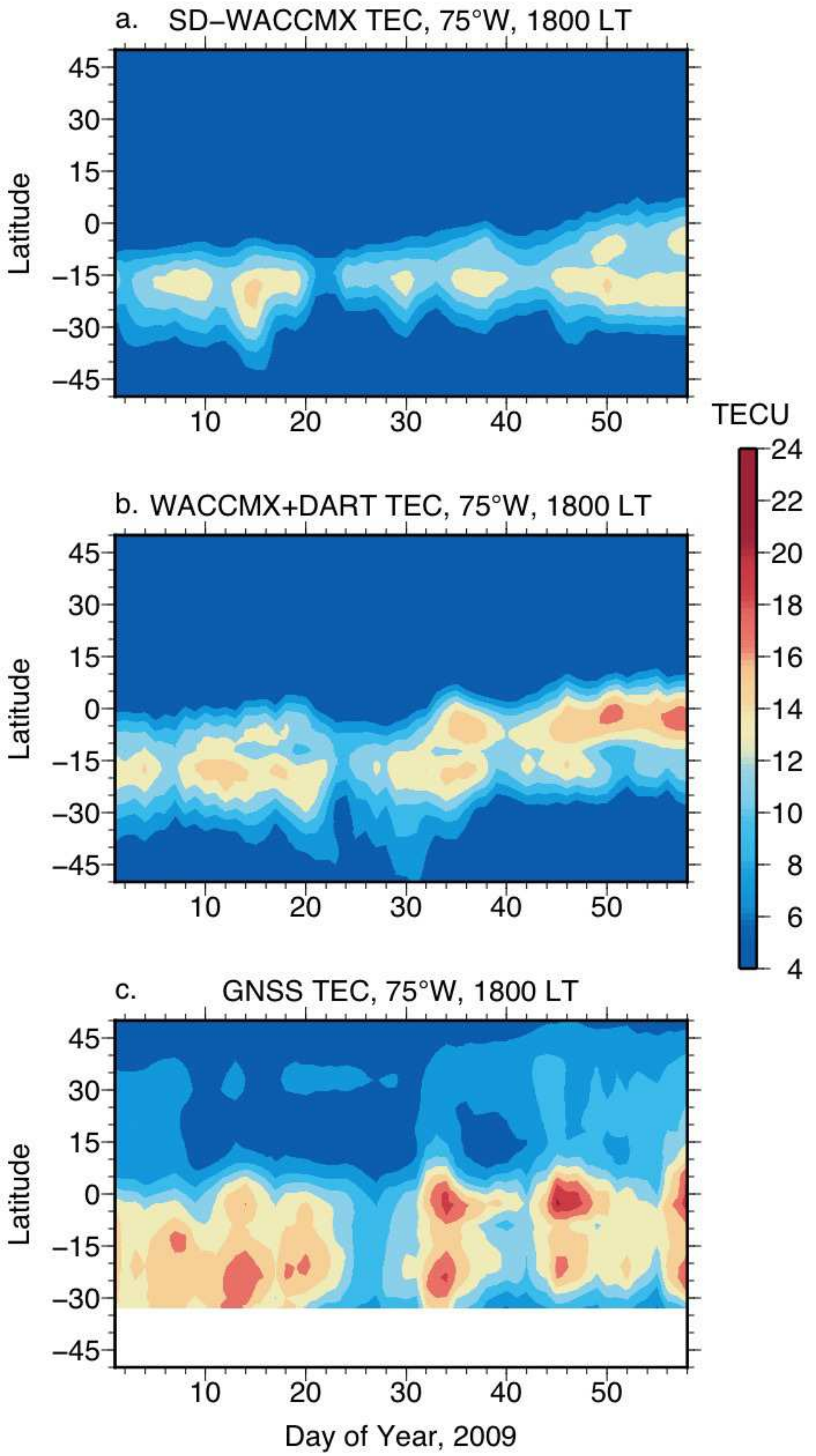

a. SD−WACCMX TEC, 75°W, 1800 LT
b. WACCMX+DART TEC, 75°W, 1800 LT
c. GNSS TEC, 75°W, 1800 LT
Latitude
45
30
15
0
−15
−30
−45
10
20
30
40
50
Day of Year, 2009
TECU
24
22
20
18
16
14
12
10
8
6
4

Figure 9.

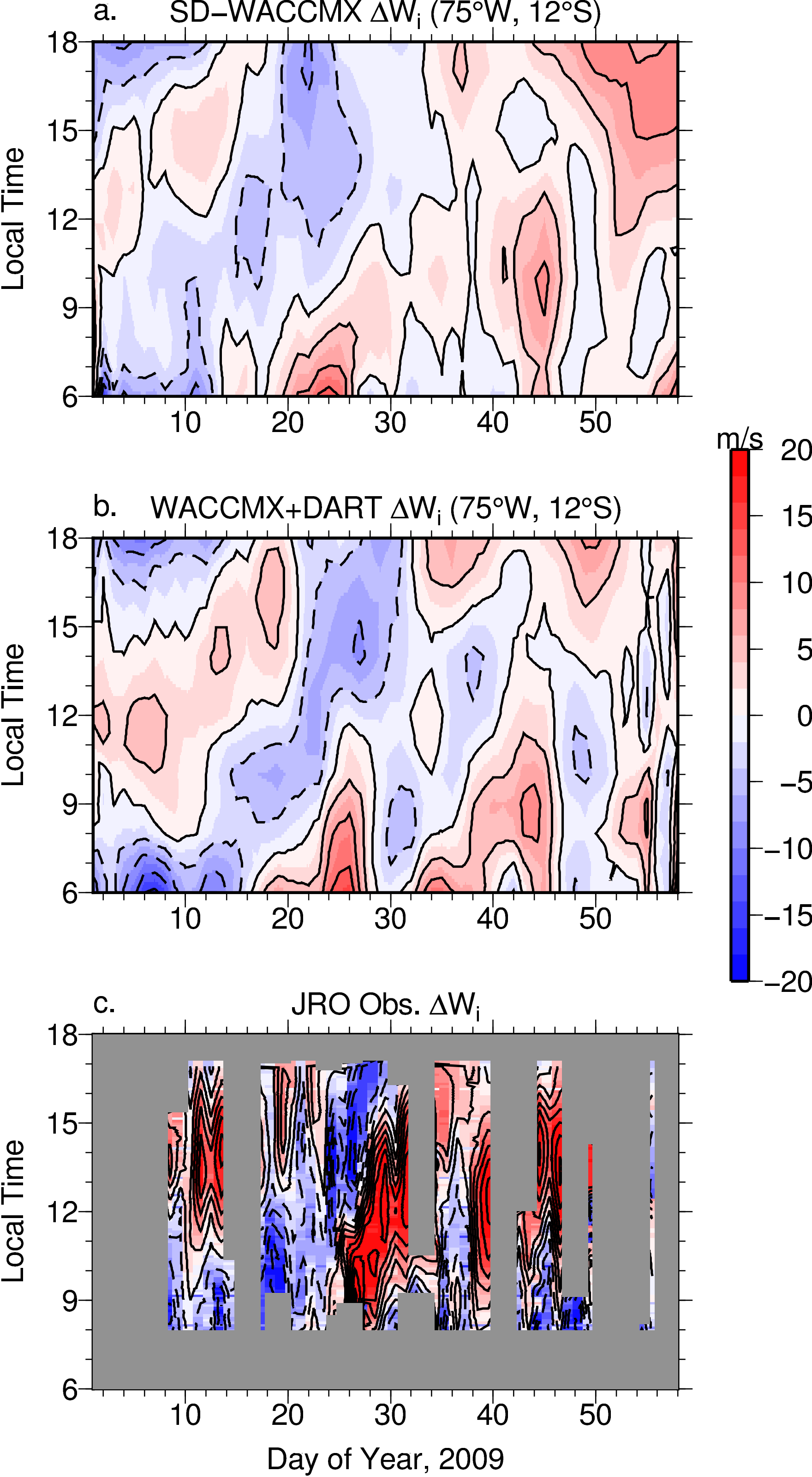

a. SD−WACCMX ΔW_i (75°W, 12°S)
b. WACCMX+DART ΔW_i (75°W, 12°S)
c. JRO Obs. ΔW_i
Local Time
6
9
12
15
18
10
20
30
40
50
Day of Year, 2009
m/s
20
15
10
5
0
−5
−10
−15
−20

Figure 10.

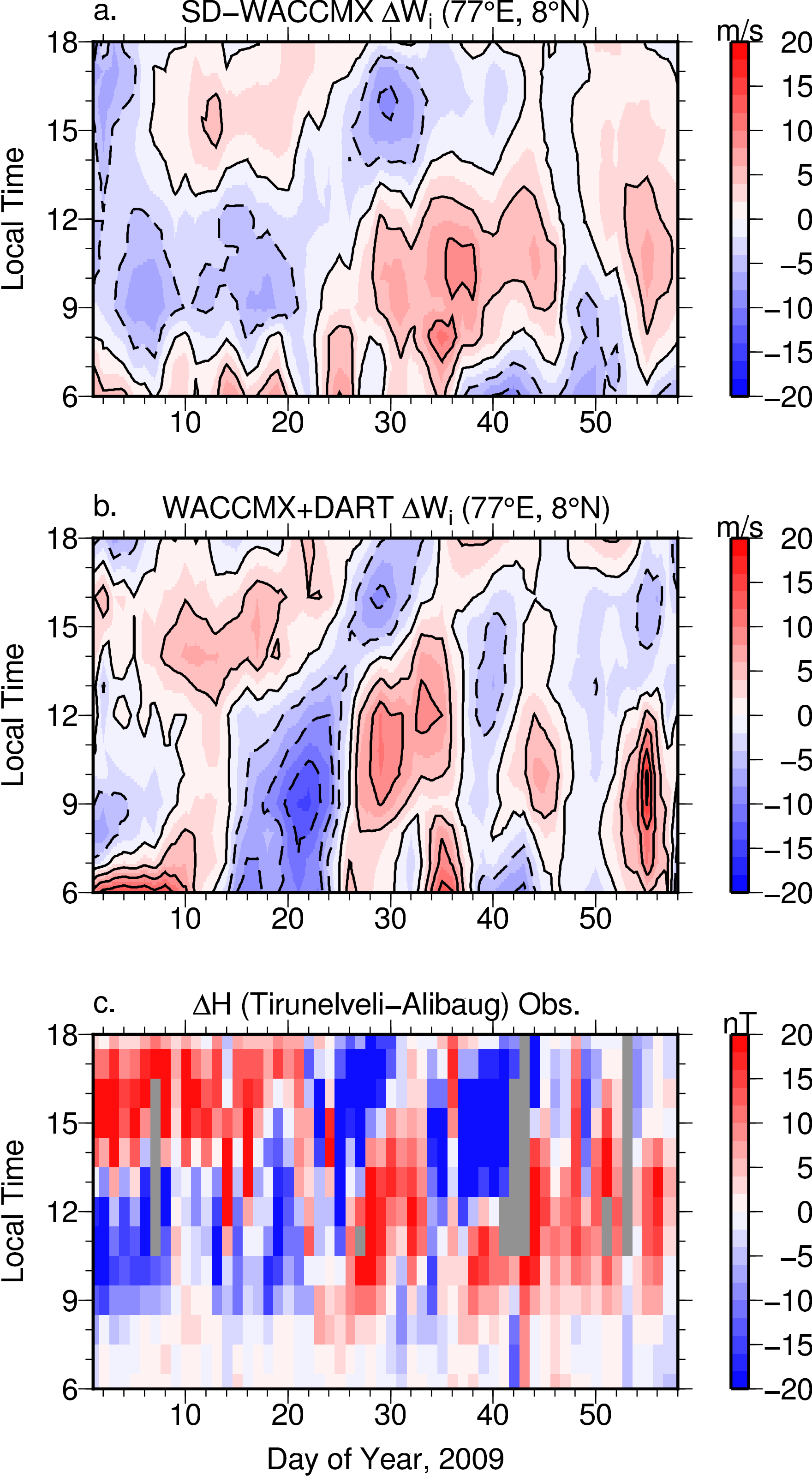

a. SD−WACCMX ΔW$_i$ (77°E, 8°N)
m/s
Local Time
b. WACCMX+DART ΔW$_i$ (77°E, 8°N)
m/s
Local Time
c. ΔH (Tirunelveli−Alibaug) Obs.
nT
Local Time
Day of Year, 2009

Figure 11.

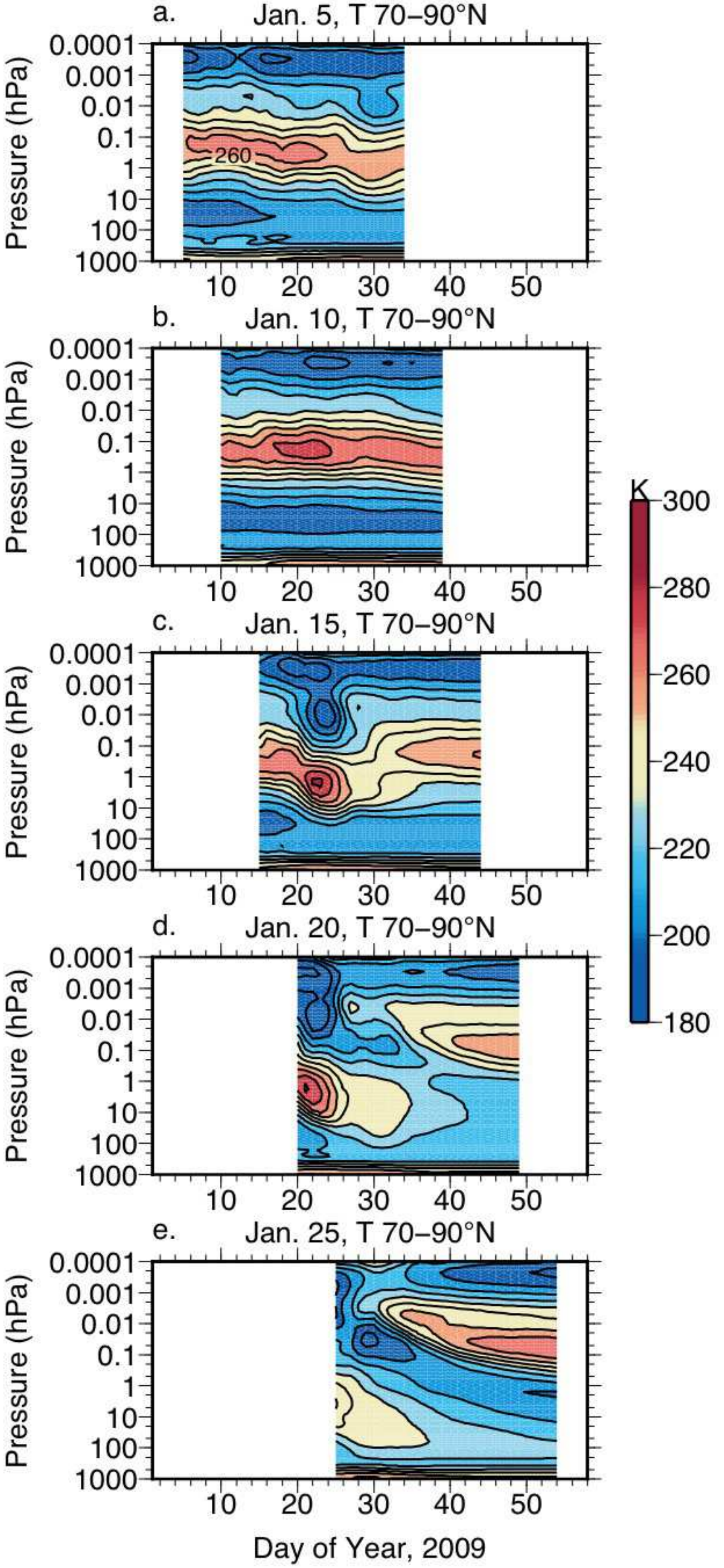
a.
Jan. 5, T 70–90°N
260
b.
Jan. 10, T 70–90°N
c.
Jan. 15, T 70–90°N
d.
Jan. 20, T 70–90°N
e.
Jan. 25, T 70–90°N
Pressure (hPa)
0.0001
0.001
0.01
0.1
1
10
100
1000
10
20
30
40
50
Day of Year, 2009
K
300
280
260
240
220
200
180

Figure 12.

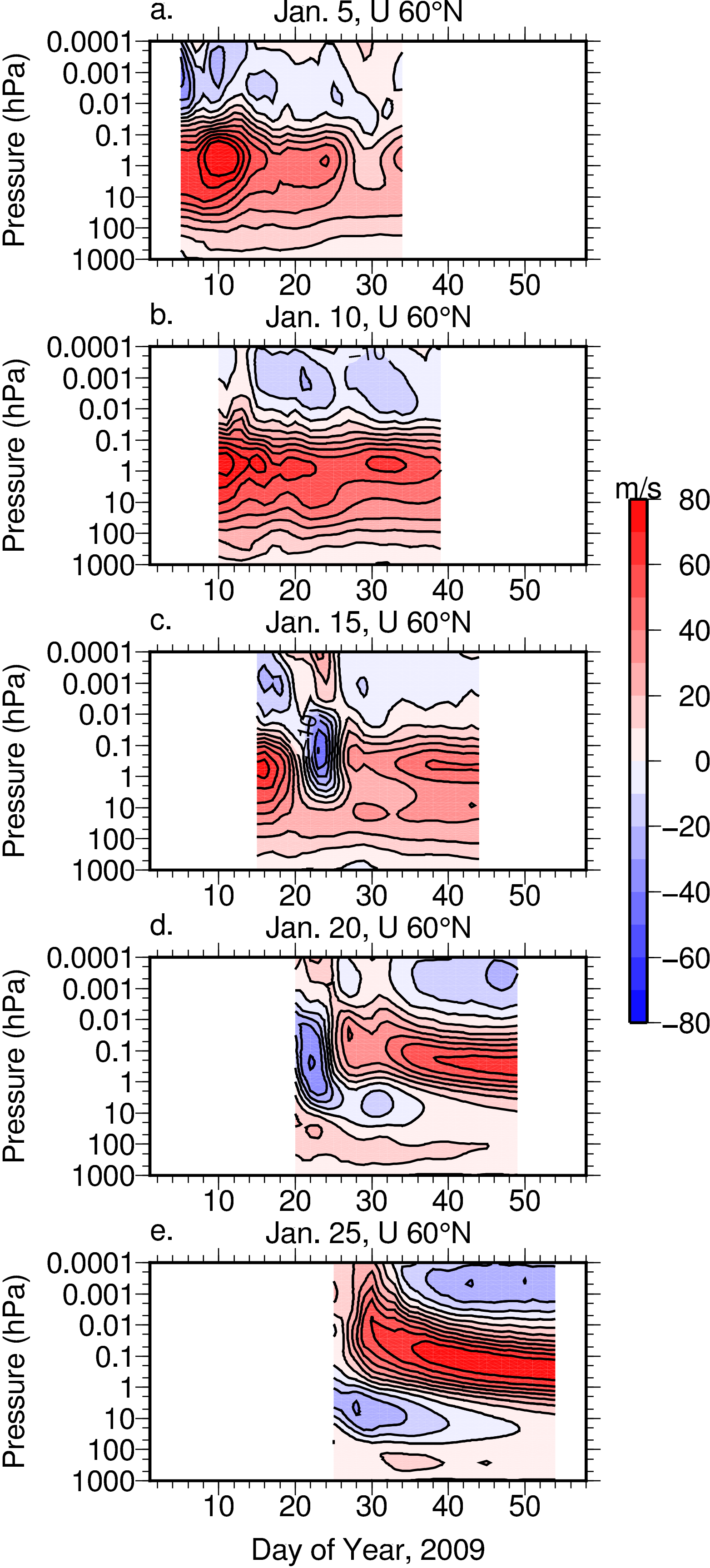
a.
Jan. 5, U 60°N
b.
Jan. 10, U 60°N
c.
Jan. 15, U 60°N
d.
Jan. 20, U 60°N
e.
Jan. 25, U 60°N
Pressure (hPa)
0.0001
0.001
0.01
0.1
1
10
100
1000
10
20
30
40
50
Day of Year, 2009
m/s
80
60
40
20
0
−20
−40
−60
−80

Figure 13.

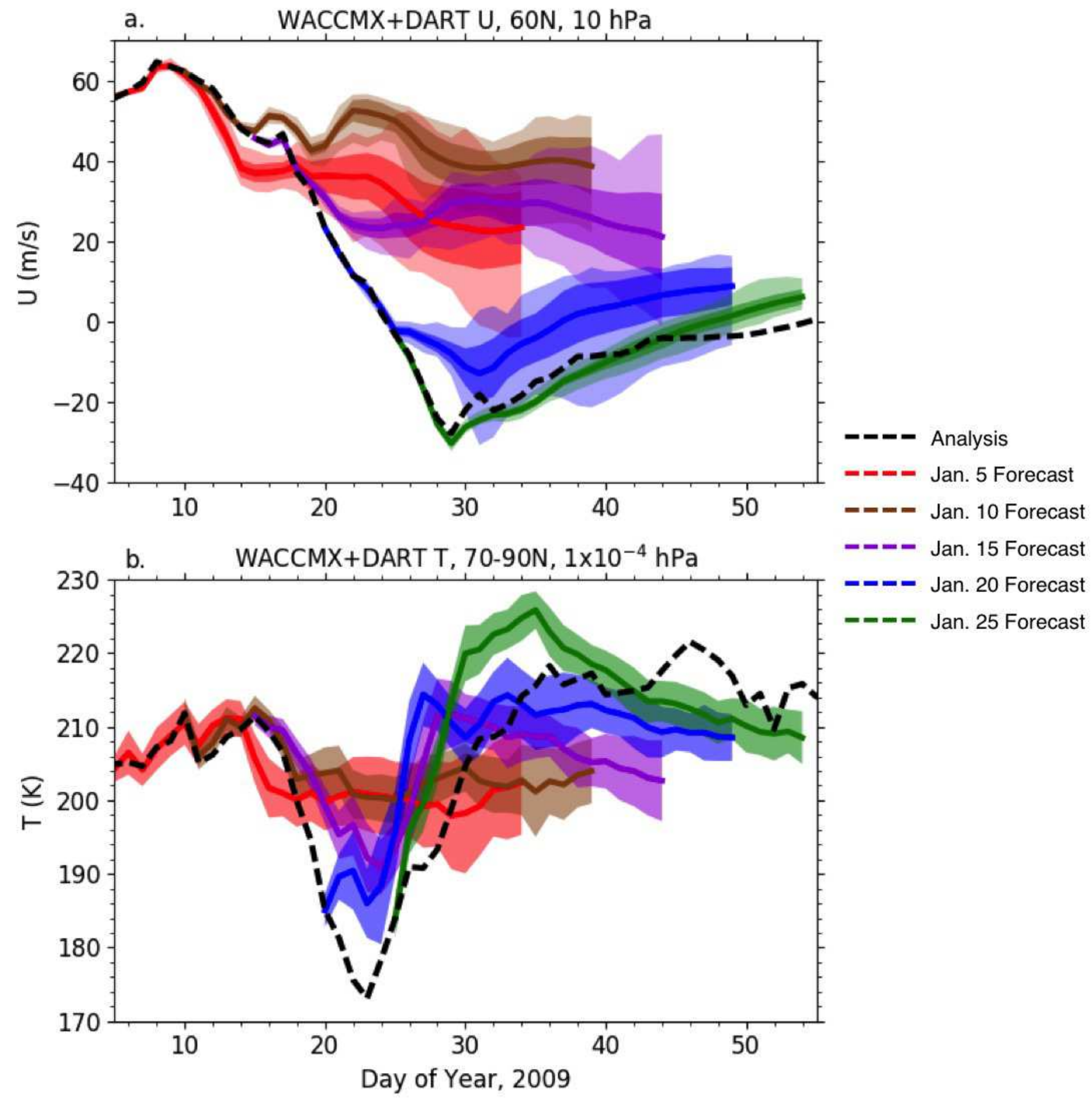
a.
WACCMX+DART U, 60N, 10 hPa
U (m/s)
60
40
20
0
−20
−40
10
20
30
40
50
Analysis
Jan. 5 Forecast
Jan. 10 Forecast
Jan. 15 Forecast
Jan. 20 Forecast
Jan. 25 Forecast
b.
WACCMX+DART T, 70-90N, 1x10^{-4} hPa
T (K)
230
220
210
200
190
180
170
10
20
30
40
50
Day of Year, 2009

Figure 14.

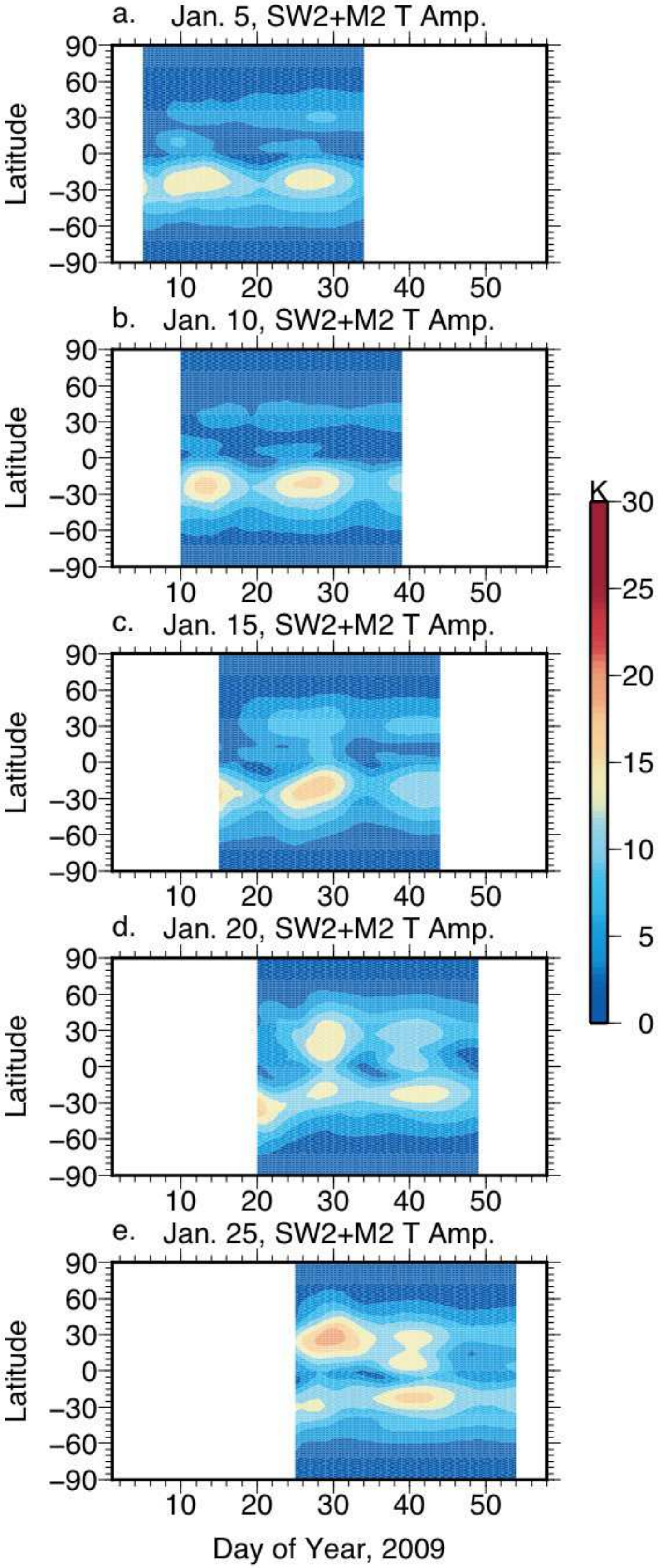

a. Jan. 5, SW2+M2 T Amp.
b. Jan. 10, SW2+M2 T Amp.
c. Jan. 15, SW2+M2 T Amp.
d. Jan. 20, SW2+M2 T Amp.
e. Jan. 25, SW2+M2 T Amp.
Latitude
90
60
30
0
−30
−60
−90
10
20
30
40
50
Day of Year, 2009
K
0
5
10
15
20
25
30

Figure 15.

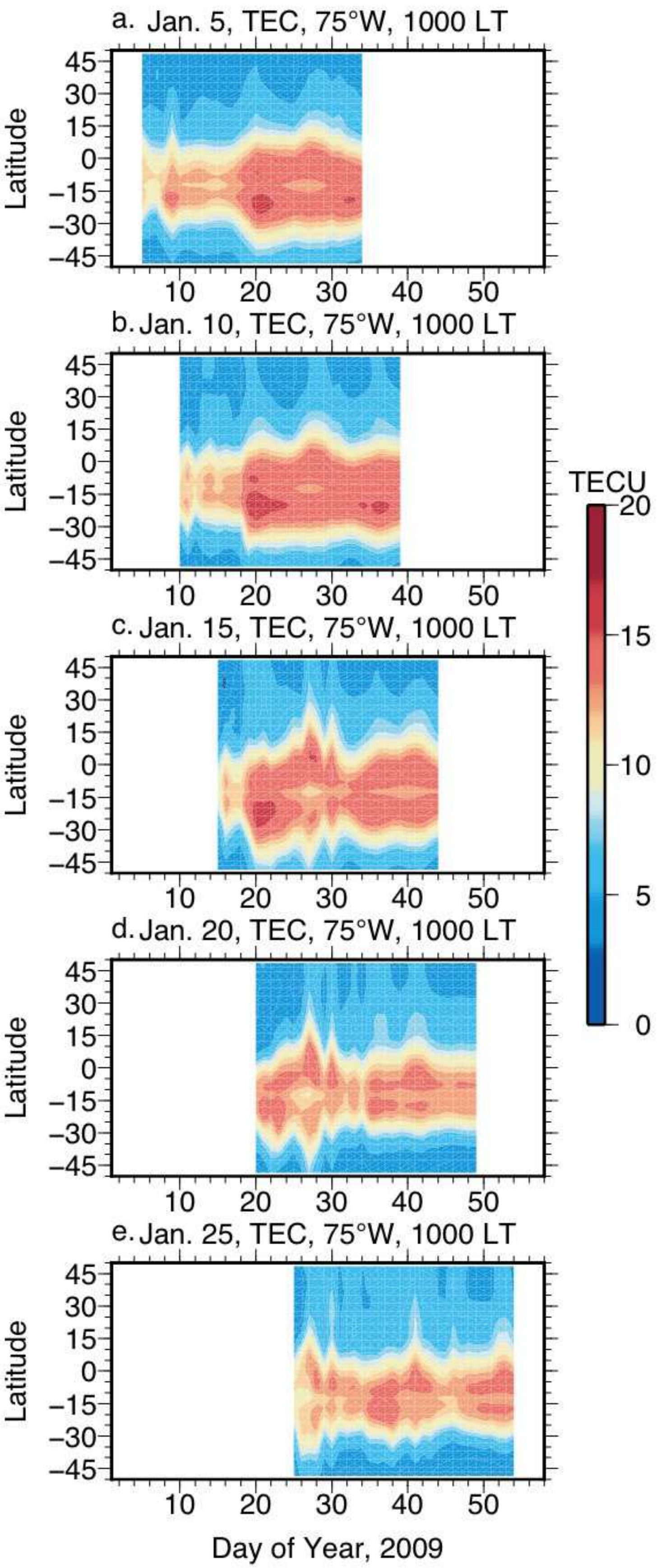

a. Jan. 5, TEC, 75°W, 1000 LT
b. Jan. 10, TEC, 75°W, 1000 LT
c. Jan. 15, TEC, 75°W, 1000 LT
d. Jan. 20, TEC, 75°W, 1000 LT
e. Jan. 25, TEC, 75°W, 1000 LT
Latitude
45
30
15
0
−15
−30
−45
10
20
30
40
50
Day of Year, 2009
TECU
20
15
10
5
0

Figure 16.

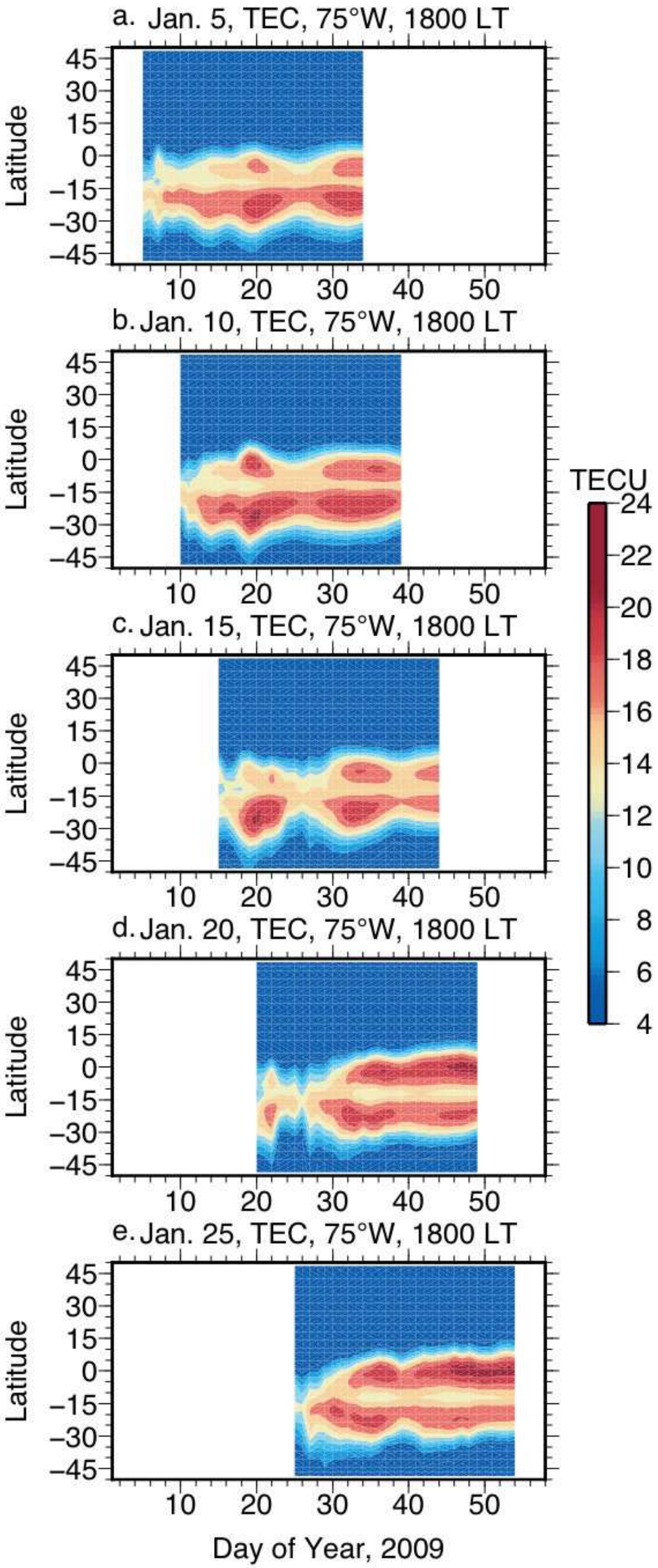

a. Jan. 5, TEC, 75°W, 1800 LT
b. Jan. 10, TEC, 75°W, 1800 LT
c. Jan. 15, TEC, 75°W, 1800 LT
d. Jan. 20, TEC, 75°W, 1800 LT
e. Jan. 25, TEC, 75°W, 1800 LT
Latitude
45
30
15
0
-15
-30
-45
10
20
30
40
50
Day of Year, 2009
TECU
24
22
20
18
16
14
12
10
8
6
4

Figure 17.

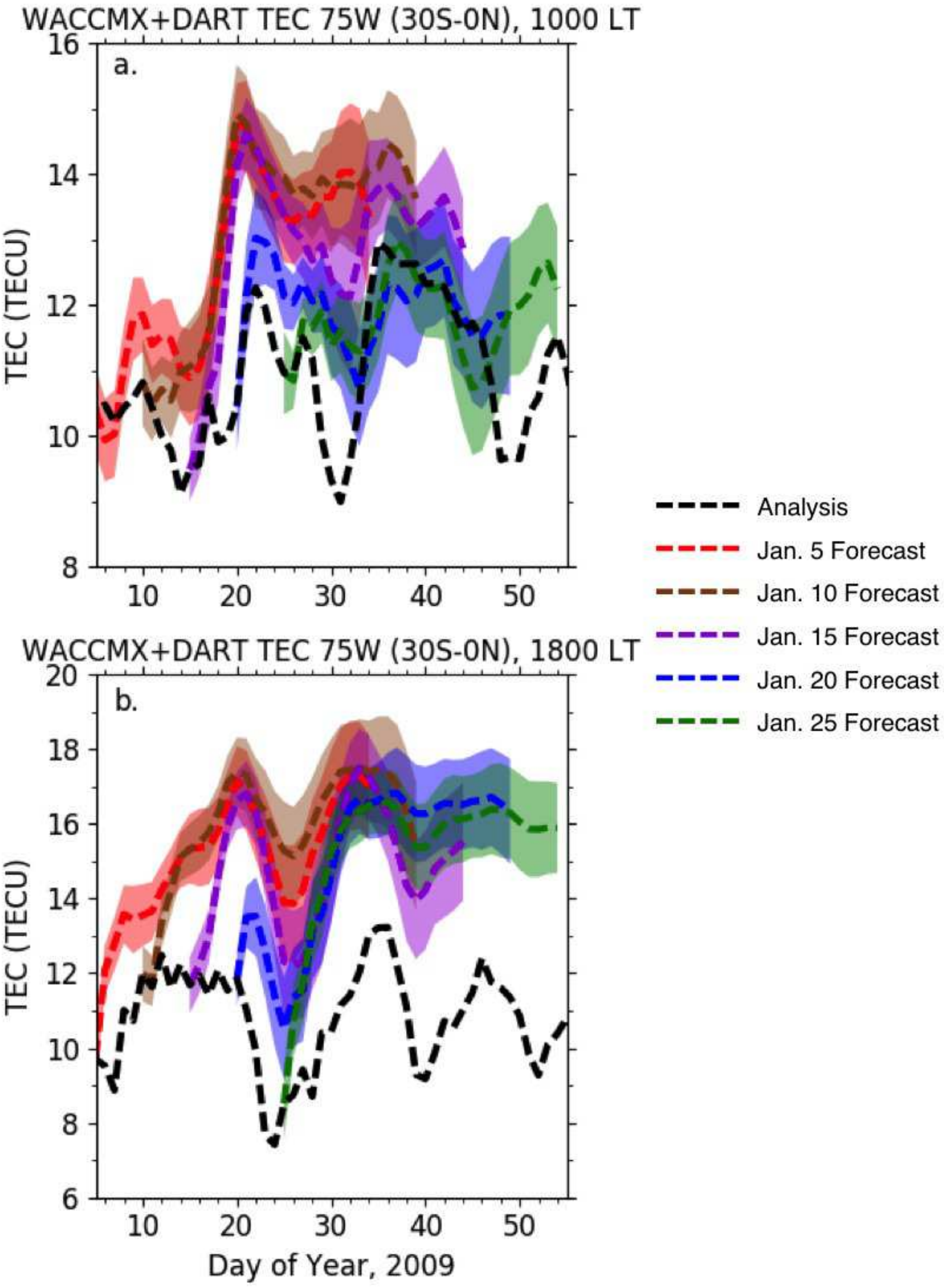
WACCMX+DART TEC 75W (30S-0N), 1000 LT
a.
TEC (TECU)
16
14
12
10
8
10
20
30
40
50
WACCMX+DART TEC 75W (30S-0N), 1800 LT
b.
TEC (TECU)
20
18
16
14
12
10
8
6
10
20
30
40
50
Day of Year, 2009
Analysis
Jan. 5 Forecast
Jan. 10 Forecast
Jan. 15 Forecast
Jan. 20 Forecast
Jan. 25 Forecast